



BRNO UNIVERSITY OF TECHNOLOGY

VYSOKÉ UČENÍ TECHNICKÉ V BRNĚ

FACULTY OF MECHANICAL ENGINEERING

FAKULTA STROJNÍHO INŽENÝRSTVÍ

INSTITUTE OF PHYSICAL ENGINEERING

ÚSTAV FYZIKÁLNÍHO INŽENÝRSTVÍ

MEV ION IRRADIATION BEAMLINE AT THE UPPSALA TANDEM ACCELERATOR: IMPROVEMENTS AND APPLICATIONS

TECHNICKÉ ÚPRAVY A APLIKACE ZAŘÍZENÍ PRO OZAŘOVÁNÍ MEV IONTY PŘI TANDEMOVÉM
URYCHLOVAČI V UPPSALE

MASTER'S THESIS

DIPLOMOVÁ PRÁCE

AUTHOR

AUTOR PRÁCE

Bc. Filip Sekula

SUPERVISOR

VEDOUCÍ PRÁCE

doc. Ing. Stanislav Průša, Ph.D.

BRNO 2021

Assignment Master's Thesis

Institut: Institute of Physical Engineering
Student: **Bc. Filip Sekula**
Degree program: Physical Engineering and Nanotechnology
Branch: no specialisation
Supervisor: **doc. Ing. Stanislav Průša, Ph.D.**
Academic year: 2020/21

As provided for by the Act No. 111/98 Coll. on higher education institutions and the BUT Study and Examination Regulations, the director of the Institute hereby assigns the following topic of Master's Thesis:

MeV ion irradiation beamline at the Uppsala Tandem Accelerator: Improvements and applications

Brief Description:

The interest in studies of ion–solid interactions and their industrial applications is rising, leading in turn to a demand for systems able to realize relevant irradiation experiments. To enable experiments with high sample throughput and good control of irradiation parameters (e.g. flux and total charge delivered to the sample, scan area, angle of incidence etc.), an experimental setup needs to be reliable and intuitive for a range of more or less experienced users. Continuous modernisation to maintain compatibility between different system components, instrumentation, control circuitry and the user workstation is also necessary.

Master's Thesis goals:

Describe the irradiation beamline at Uppsala University's Tandem Laboratory.

Implement improvements to sample transfer system mechanism at the beamline.

Re-design and replace the transfer system control circuit.

Rewrite control software and design user interface for irradiation experiments.

Describe the response of a material to irradiation in a few practical cases, connect the physics of ion-solid interactions and experimental outcomes.

Predict the lateral homogeneity of the ion fluence received by a sample when irradiating with a beam deflected by a time-varying electric field whose components in two perpendicular directions have different frequency and amplitude.

Recommended bibliography:

HOROWITZ, Paul and Winfield HILL. 2015. The art of electronics. Third edition. New York: Cambridge University Press.

NASTASI, Michael, James MAYER and James K. HIRVONEN. 1996. Ion-Solid Interactions: Fundamentals and Applications. Cambridge: Cambridge Solid State Science Series.

HALLÉN, Anders, P. Anders INGEMARSSON, Per L. HÄKANSSON, Bo U.R. SUNDQVIST and Göran POSSNERT. 1989. An MeV-ion implanter for large area applications. Nuclear Instruments and Methods in Physics Research Section B: Beam Interactions with Materials and Atoms. 36(1), 345-349.

Deadline for submission Master's Thesis is given by the Schedule of the Academic year 2020/21

In Brno,

L. S.

prof. RNDr. Tomáš Šikola, CSc.
Director of the Institute

doc. Ing. Jaroslav Katolický, Ph.D.
FME dean

Abstract

The MeV ion irradiation beamline at Uppsala University's Tandem Laboratory is presented in this thesis. Theoretical basics of ion-solid collisions are discussed and material modification of solids by impinging energetic ions is described. The Tandem Accelerator setup is described starting from ion generation and ending with ions impinging on sample in irradiation beamline's main chamber. The sample transfer system is presented alongside improvements and modifications implemented to the original setup. A pilot application of improved system in material modification is presented on Ge quantum dot irradiation and ion fluence uniformity is analyzed using an electrostatic deflector simulation.

Abstrakt

V této práci je představeno zařízení pro ozařování MeV ionty při tandemovém urychlovači na univerzitě v Uppsale. Jsou podány základy teorie interakce iontů s pevnou látkou a modifikace materiálu pomocí iontů s vysokou energií. Zařízení tandemového urychlovače je popsáno počínaje generací iontů a konče dopadem iontů na vzorek v hlavní komoře zařízení pro iontové ozařování. Následně jsou detailně charakterizovány modifikace systému pro přesun vzorků a popsán princip jeho funkce. Pilotní aplikace upraveného systému v oblasti materiálových modifikací je prezentována na příkladu ozařování Ge kvantových teček. Homogenita rozložení iontů na vzorku při ozařování je testována pomocí simulace elektrostatického deflektoru.

Keywords

Ion irradiation, Ion physics, Tandem accelerator, Material modifications by ion beam, MeV ions, Ion optics, Sample transfer system

Klíčová slova

Ozařování ionty, Iontová fyzika, Tandemový urychlovač, Modifikace materiálu iontovým svazkem, MeV ionty, Iontová optika, Systém přesunu vzorků

Extended abstract in Czech

Tato práce se věnuje zařízení pro ozařování MeV ionty při tandemovém urychlovači na univerzitě v Uppsale, popisu technických úprav a ukázce jeho aplikace v materiálových vědách. Výhodou tohoto zařízení je možnost ozařování velkoplošných vzorků o rozměrech až $(10 \times 10) \text{ cm}^2$, což umožňuje modifikaci celých čtyřpalcových waferů. Další předností zařízení je možnost skladovat až 20 vzorků o těchto rozměrech ve vakuu a jejich ozařování bez nutnosti zavzdušňování komory mezi ozařováním jednotlivých vzorků.

Úvodní kapitola práce se věnuje interakci iontů s pevnou látkou. Tato interakce je popsána od interakčního potenciálu, přes stínící funkce zahrnující vliv elektronů až po teorii binární kolize částic, která charakterizuje změnu energie částic během kolize při dané geometrii srážky. Dále je zmíněn diferenciální účinný průřez popisující úhlové rozložení částic po srážce v závislosti na hodnotě srážkového parametru. Vliv krystalické struktury materiálu na trajektorii částice je charakterizován pomocí "kanálování", které označuje anglický termín "channeling". Hloubka vniku částic do materiálu je definována pomocí energie odevzdané během pohybu částice materiálem, iontového brzdného účinku ("ion stopping"). Tato teorie je poté využita k popisu materiálové modifikace iontovým svazkem. Kapitola je uzavřena aplikacemi iontového ozařování v materiálových vědách.

Následující část textu je věnována instrumentaci zařízení pro ozařování MeV ionty. V injekčním systému jsou ve čtveřici iontových zdrojů generovány negativní ionty, které jsou následně injektovány do tandemového urychlovače částic, kde dochází k jejich urychlení na požadovanou energii. Negativní ionty jsou v urychlovači urychleny směrem k prostoru s inertním argonovým plynem, kde dojde k jejich změně na ionty pozitivní, které jsou opětovně urychleny a putují směrem k filtračnímu magnetu, nímž projdou jen částice o požadované energii a specifickém náboji. Svazek je poté fokusován a nasměrován přepínacím magnetem do ozařovacího zařízení. V tomto zařízení je svazek rozkmitán dvojicí na sebe kolmých elektrostatických deflektorů a skenován po povrchu vzorku v hlavní komoře. Je zde i stínítko pro zamezení průchodu svazku. Přesun vzorků mezi hlavní komorou a vedlejší komoru, kde je umístěn zásobník se vzorky, realizuje transportní systém. Princip funkce transportního systému je detailně popsán. Jsou představeny jeho dvě základní části, transportní rameno a zásobník vzorků. Dále je ukázáno konstrukční řešení držáků vzorků a realizace jejich transportu mezi zásobníkem a hlavní komorou, kde dochází k ozařování vzorků.

Transportní systém přešel od první verze zařízení pro MeV ozařování ionty v roce 1989 několika úpravami. Popis poslední z těchto úprav realizované v roce 2020 je obsažen v této práci. Jsou představeny změny mechanismu pro úchop vzorků, které přinesly zvýšenou spolehlivost transportu vzorků a eliminovaly neduhy předchozí varianty (naklánění a vypadávání vzorků), které často způsobily přerušení experimentu. Další změnou byla výměna původní ovládací jednotky komunikující s počítačem pomocí programovatelného logického ovladače (PLC) za novou jednotku, která byla navržena tak, aby zachovala původní funkcionalitu a umožnila připojení k moderním počítačům (původní systém řízení byl omezen limity operačního systému Windows 95). Pro implementovanou ovládací jednotku bylo nutné napsat novou řídicí aplikaci, která realizuje transport vzorků a výpočet času potřebného pro dosažení požadované ozařovací dávky pro zadané parametry systému.

Modernizované zařízení bylo poté otestováno v pilotním experimentu, jehož cílem bylo zvýšení fotoluminiscence germániových kvantových teček vlivem defektů způsobených

ných iontovým ozařováním. Vzorky byly po ozáření ionty uhlíku a chlóru o různých energiích a ozařovacích dávkách odeslány zpět na Johannes Kepler University Linz (kde byly vyrobeny) na měření fotoluminescence. Z měření vyplynulo, že použité ionty nejsou vhodné pro tuto modifikaci materiálových vlastností, jelikož způsobily téměř lineární pokles intenzity fotoluminescence v závislosti na ozařovací dávce.

Distribuce iontů byla na závěr otestována pomocí počítačové simulace. Gaussovsky prostorově rozdělené částice byly vychylovány pomocí modelu elektrostatického deflektoru a výsledné rozložení částic v rovinně vzorku bylo kontrolováno na přítomnost pravidelných stop vzniklých vlivem použitých frekvencí pro jednotlivé směry vychýlení elektrostatickým deflektorem. Plošná a časová homogenita byla úspěšně ověřena. Rozložení bylo také úspěšně testováno pro několik hodnot proudu v primárním svazku.

Modifikace zařízení neovlivnily negativně jeho fyzikální vlastnosti a homogenita ozařování je stále zachována. Implementované úpravy zjednodušují obsluhu zařízení a částečně automatizují jeho chod. Dalším krokem v modernizaci zařízení je přidání funkce automatického ozařování vzorků, při kterém by uživatel volil vzorky, které mají být ozářeny a následně také expozici (dávku). Tento krok by umožnil realizovat dlouhé série ozařování bez nutnosti přítomnosti personálu po celou délku experimentu a manuální manipulace s jednotlivými vzorky.

SEKULA, Filip. *MeV ion irradiation beamline at the Uppsala Tandem Accelerator: Improvements and applications*. Brno, 2021. Master's thesis. Brno University of Technology, Faculty of Mechanical Engineering, Institute of Physical Engineering. Supervised by Stanislav Průša.

I hereby declare that I am the sole author of this master thesis and that I have not used any sources other than those listed in the bibliography and identified as references. I further declare that I have not submitted this thesis at any other institution in order to obtain a degree.

Filip Sekula

First of all I would like to thank my supervisor, Stanislav Průša, for making this work possible. Without him, this project would never happen and I would not have this life changing experience in the north.

Next I would like to thank everyone at Uppsala University's Tandem Laboratory for their warm welcome and the home like atmosphere at the workplace. I will deeply miss our shared fikas. I especially want to thank Daniel Primetzhofer, Petter Ström and Jonas Åström for all the support they provided. Without their help, insight and tips this work would not have reached it's finishing line in the short time we had during my Erasmus stay.

My next thanks is directed to Linz to Lukas Spindlberger for providing the photoluminescence data and help with their interpretation and noting the interesting physics involved.

I would also like to thank Marcel Janák, Radek Holeňák for the moral support and survival tips to make it through the half year in the unforgiving north and Petr Liška for his help and support during the writing of this thesis.

Last but not least I would like to thank my family and friends for their continued support during my studies. I would not have made it this far without you.

This work was realised with financial support from European Union programme for education Erasmus+.

Filip Sekula

Contents

1	Introduction	1
2	Ion irradiation	3
2.1	Ion-solid interaction	3
2.1.1	Interaction potential	3
2.1.2	Screening function	4
2.1.3	Binary collision	4
2.1.4	Differential cross-section	5
2.1.5	Channeling	6
2.2	Ion stopping	7
2.2.1	Ion range	8
2.3	Ion irradiation damage	8
2.3.1	Ion induced displacement	9
2.3.2	Deposited energy	10
2.4	Applications	10
3	Irradiation beamline instrumentation	11
3.1	Accelerator setup	11
3.1.1	Ion injection system	11
3.1.2	Tandem accelerator	13
3.1.3	Beam formation system	13
3.2	Irradiation beamline	15
3.2.1	Deflection unit	15
3.2.2	Shutter	16
3.2.3	Main chamber	16
3.2.4	Chamber vacuum	18
4	Sample transfer system: Modifications and improvements	19
4.1	Sample transfer system	20
4.1.1	Sample holders	20
4.1.2	Shuttle	21
4.1.3	Magazine	23
4.2	Grip improvements	24
4.3	Control unit replacement	25
4.3.1	Shutter control	26
4.3.2	Shuttle position measurement	26
4.3.3	Shuttle movement	27
4.3.4	Magazine movement	29

4.3.5	Sensor circuit	29
4.3.6	Grip control	31
4.3.7	Control unit housing	31
4.4	T5 Control software	31
4.4.1	Shuttle control	33
4.4.2	Magazine control	34
4.4.3	Irradiation control	34
4.4.4	Chamber pressure	35
4.4.5	Trouble shooting	35
4.4.6	Batch planner	36
4.4.7	Future modifications	37
5	Germanium quantum dot irradiation	39
5.1	Sample irradiation	39
5.1.1	Sample preparation	39
5.1.2	Irradiation parameters	40
5.2	Photoluminescence measurements	40
5.2.1	Results	41
6	Irradiation homogeneity	45
6.1	Theoretical model	45
6.2	Results	48
7	Conclusions	53
	References	55
	List of abbreviations	59
	List of attachments	61

1. Introduction

The MeV ion irradiation beamline at Uppsala University has been first presented in 1989 [1], and has been running irradiation experiments ever since. Its most notable features, the large irradiation area of up to $(10 \times 10) \text{ cm}^2$ and magazine able to accommodate up to 20 sample holders of such area, have been used from its first irradiation runs up to this day. The setup has undergone many changes in the past; its most recent iteration is presented in the following text.

In the beginning we will delve into the theory of ion irradiation. We will start at ion-solid interaction, where the interactions potential, screening function and binary collision theory be briefly introduced followed by differential cross-section and channeling effect. Then we will move on to ion stopping and how the penetration depth of an ion in a solid, the ion range, is described. The last part of the theoretical background consists of ion irradiation damage and how the impinging ions can modify the irradiated material. The entire chapter will be closed by a brief presentation of possible applications of ion irradiation.

The next part of the text is dedicated to irradiation beamline setup. We will begin at accelerator setup following the path of the ion from its creation and extraction at an ion source continued by its injection to tandem accelerator, where the ion is accelerated, and ending at beam formation system, where the desired energy is chosen and the ion is sent towards the irradiation beamline. The key components of the irradiation beamline, deflection unit and shutter, will be introduced before we move on to the main chamber, where the irradiation of samples is realised and where the sample transfer system is located. Last but not least the beamline's vacuum system will be mentioned.

The following chapter will show the aforementioned sample transfer system in its current state. Its main components, shuttle and magazine, will be described in detail alongside used sample holders. Then we move onto the modifications and improvements implemented to the system. The shuttle's improved grip mechanism will be presented and compared with the previous iteration. Next, the control unit replacement, will be shown in detail accompanied by the rewritten T5 control software realised in LabView [2] and description of its functions.

A pilot experiment on the newly improved system will be presented in the next chapter. The germanium quantum dots irradiation experiment to improve the quantum dot photoluminescence will be described from the sample preparation before irradiation to irradiation itself followed by photoluminescence measurement results.

The last chapter will deal with the main parameter of irradiation experiments, the irradiation homogeneity. The electrostatic deflection system used at the irradiation

beamline will be simulated using MATLAB software [3] and effects of ion flux and sweep frequencies on irradiation homogeneity will be discussed.

2. Ion irradiation

When we are talking about ion irradiation, we mean a flux of energetic ions impinging on a surface of a solid. The goal of an irradiation experiment is often to change properties of the irradiated material, which can be achieved in a variety of ways. But before we start talking about how and why the material is modified, we need to start on the surface and slowly delve deeper into the interactions of projectiles coming in contact with the bombarded solid.

2.1 Ion-solid interaction

Our delve will begin with two ions, how they interact with each other and what role electrons play in it. Then we will discuss the possible outcomes of charged particle collisions and influence of material's structure on particle trajectories.

2.1.1 Interaction potential

We start our description of atom interaction using only their nuclei, neglecting the influence of electrons at the moment. Such interaction can be described using Coulomb potential

$$V_C = -\frac{Z_1 Z_2 e^2}{r} \quad (2.1)$$

where

$$e^2 = \frac{e_{\text{SI}}^2}{4\pi\epsilon_0} = 1.44 \text{ eV nm} \quad (2.2)$$

is elementary charge in CGS system, which will be used henceforth unless stated otherwise, e_{SI} is elementary charge in SI system, Z_1 , Z_2 are atomic numbers of interacting nuclei and r is separation between them [4].

The force between the particles is then given by Coulomb force

$$F_C = -\frac{d}{dr}[V_C(r)] = \frac{Z_1 Z_2 e^2}{r^2} \quad (2.3)$$

giving us the magnitude of repulsive force between the nuclei. If we take influence of electrons into consideration the Coulomb potential changes into

$$V_C = -\frac{Z_1 Z_2 e^2}{r} \chi(r) \quad (2.4)$$

where the newly added $\chi(r)$ is screening function describing contribution of electrons to nuclei interaction [4]. This potential is called screened Coulomb potential.

2.1.2 Screening function

The electrons in inner atomic orbitals influence the nuclei interaction by lowering the Coulomb potential. This effect is described by screening function $\chi(r)$. At long distance the negative space charge of the electrons screens the positive nuclei, lowering the repulsive force. With decreasing distance screening becomes negligible.

The screening function is a solution of Thomas-Fermi equation originating from a model of atom with the same name, where electrons behave like an ideal gas and can be treated by Fermi-Dirac statistics. An accurate solution of Thomas-Fermi screening function is realized by numerical methods, with a typical solution in form of series [4].

For applications in experiments where high precision is not desired, analytical approximations of Thomas-Fermi screening function are used. These functions are created by fitting the numerical data with analytical functions. Many forms of approximate screening functions exist beginning from Sommerfeld and Kerner models to Lindhard and Moliere models, with the last mentioned giving the screening function of a nucleus as

$$\chi(r) = 0.35 \exp(-0.3x) + 0.55 \exp(-1.2x) + 0.10 \exp(-6.0x) \quad (2.5)$$

with x defined as

$$x = \frac{r}{a_{\text{TF}}} \quad (2.6)$$

where

$$a_{\text{TF}} = \frac{1}{2} \left(\frac{3\pi}{4} \right)^{\frac{3}{2}} \frac{\hbar^2}{m_e e^2 Z^{\frac{1}{3}}} = \frac{0.885 a_0}{Z^{\frac{1}{3}}} \quad (2.7)$$

is Thomas-Fermi screening length, $a_0 = \hbar^2/(m_e e^2)$ is Bohr radius and m_e is mass of electron [4].

2.1.3 Binary collision

The collisions of projectile ions with target atoms of solid can be described by elastic binary collision theory. To explain this theory we have to start with assumptions that are used. Only two-atom collisions are considered and classical dynamics are used. The inelastic effects such as electron excitation and ionization only cause energy losses, but do not influence collision dynamics, and one of the two colliding atoms, target atom in our case, is initially at rest.

The kinematics of elastic binary collision, or scattering for short, can then be derived from energy and momentum conservation laws to give a formula describing energy loss of an projectile atom scattered on a stationary target atom depicted in Figure 2.1

$$\frac{E_1}{E_0} = \left[\frac{\pm (M_2^2 - M_1^2 \sin^2 \theta)^{1/2} + M_1 \cos \theta}{M_1 + M_2} \right]^2 \quad (2.8)$$

where E_0 and E_1 are projectile energies before and after the scattering respectively, M_1 and M_2 are masses of projectile and target atom and θ is scattering angle as seen in Figure 2.1 [4]. The right hand side of the equation is called the kinematic factor. The energy lost by the projectile is transferred on to the target atom and its value is determined from energy conservation law as $E_2 = E_0 - E_1$. The direction of target atom's movement can then be determined from momentum conservation law, giving the angle ϕ .

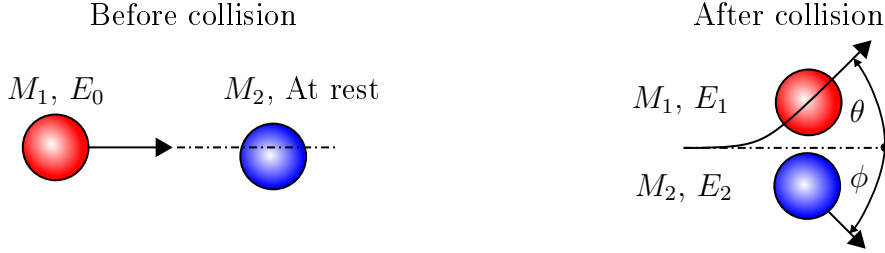


Figure 2.1: Binary collision of two atoms. (Left) Atoms before the collision. The projectile with energy E_0 is approaching the stationary atom. (Right) After collision. The projectile was scattered by target atom and travels on a linear trajectory tilted by angle θ from original trajectory with energy E_1 . The target atom started moving on a linear trajectory tilted by angle ϕ with energy E_2 .

2.1.4 Differential cross-section

While the kinematic factor gives the energy preserved by the projectile when scattering towards a certain angle θ , the differential cross section gives the ion's probability to scatter towards that angle. We begin with a total scattering cross-section

$$\sigma(\theta) = \pi b^2 \quad (2.9)$$

dependent on scattering angle θ as shown in Figure 2.2. Differentiating $\sigma(\theta)$ gives us

$$d\sigma = 2\pi b db. \quad (2.10)$$

When an ion with an impact parameter in interval $b + db$ approaches a target atom, it will get scattered in a range of scattering angles $\theta + d\theta$ relative to its original trajectory. The dependence of impact parameter b on scattering angle θ allows us to rewrite Equation 2.10 as

$$d\sigma = 2\pi b(\theta) \left| \frac{db(\theta)}{d(\theta)} \right| d(\theta). \quad (2.11)$$

Since geometry of such collision is rotationally symmetrical, we can determine the solid angle using Figure 2.2 as

$$d\Omega = 4\pi \frac{dA}{A} = 4\pi \frac{2\pi(R \sin \theta)(Rd\theta)}{4\pi R^2} = 2\pi \sin \theta d\theta. \quad (2.12)$$

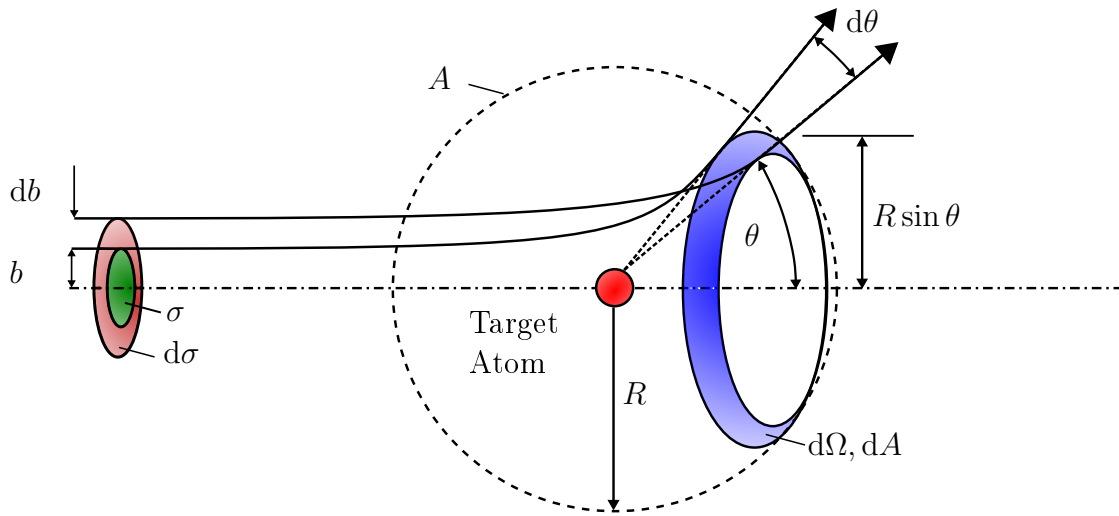


Figure 2.2: Geometry of differential cross-section. Projectiles with impact parameter from b to $b + db$ are scattered by target atom at angles from $\theta + d\theta$ to θ . Using a reference sphere of radius R and area A a solid angle $d\Omega$, denoted by blue area dA on the reference sphere, can be calculated using the definition of solid angle.

The differential cross-section can then be defined as

$$\frac{d\sigma(\theta)}{d\Omega} = \frac{b}{\sin\theta} \left| \frac{db}{d\theta} \right| \quad (2.13)$$

The differential cross-section tells us the probability that a projectile will be scattered to a solid angle $d\Omega$ [4]. If n ions impinge on a scattering center defined by a differential cross-section, we can predict the amount of ions scattered in solid $d\Omega$ as

$$n \frac{d\sigma(\theta)}{d\Omega} \quad (2.14)$$

In material analysis, differential cross-section can be used to find the optimal angle of detectors to maximize the amount of detected ions, allowing for more efficient measurements.

2.1.5 Channeling

If projectile doesn't get backscattered upon collision with target atoms on the very surface, it can undergo multiple elastic binary collisions in target's body. Such collision cascade then ends when projectile loses all of its kinetic energy or when it leaves the material before its energy is depleted. There is another possibility that can happen to a projectile approaching the target. This possibility is called channeling.

In channeling, ions travel through a channel between atomic strings of target material as shown in Figure 2.3, allowing for much deeper penetration of projectiles into

target. These channels exist in crystalline materials only and only alongside certain crystallographical axes, for example in Si alongside $\langle 100 \rangle$ axis.

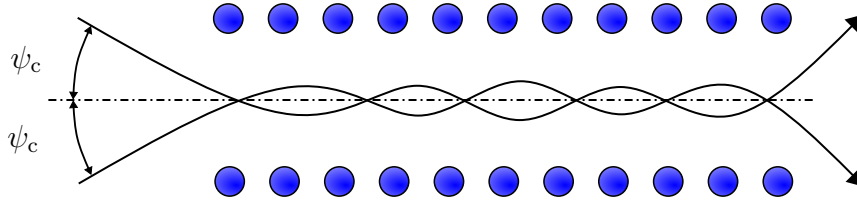


Figure 2.3: Channeling in crystalline material. Ions entering channel under angles smaller than ψ_c are channeled deeper into the material.

For channeling to occur, the sample's channels must be aligned at angle smaller than or equal to critical angle ψ_c with respect to impinging ion beam. The critical angle depends on projectile energy, projectile species and target material, but for most ion-target combinations the critical angle is approximately 5° . To minimize unwanted channeling, samples are mounted at angles greater than 7° [4].

2.2 Ion stopping

An energetic ion impinging upon solid that is not backscattered on solid's surface, penetrates the solid and loses energy by interaction with atoms and electrons inside the material. In these collisions the incident particle loses energy over path travelled in solid at a rate of dE/dx of a few eV to 10 keV per nanometer [4, 5]. The penetration depth, or simply ion range, R can then be determined as distance upon which the ion loses all its energy

$$R = \int_{E_0}^0 \frac{1}{dE/dx} dE \quad (2.15)$$

where E_0 is ion's initial energy.

The rate of particle energy loss per unit length dE/dx is known as the stopping power in the material and is expressed by formula

$$\frac{dE}{dx} = \frac{dE}{dx}|_n + \frac{dE}{dx}|_e \quad (2.16)$$

where n stands for nuclear stopping and e is electronic stopping. The nuclear stopping comes from projectile's interaction with nuclei in the solid. The energy loss is a collective effect of many small angle collisions with large impact parameters. Collisions with nuclei also induce atom displacements in target lattice. The electronic stopping on the other hand comes from the interaction between ion and electrons in solid. These electronic collisions cause energy losses and scattering at negligible scattering angles. The nuclear stopping dominates at lower projectile energies and heavier projectile species. For higher energies and lighter projectiles the electronic stopping prevails [4].

Another way to describe ion stopping is stopping cross-section S defined as

$$S \equiv \frac{dE}{dxN} \quad (2.17)$$

where N is atomic density. S expresses ion stopping per atom in the volume of solid.

An extensive database of ion stopping values for plethora of projectile-target combinations is available [5]. The Stopping and Range of Ions in Matter software, SRIM, provides variety of useful features like ion stopping and ion range calculations, that can be used to predict experimental results [6, 7].

2.2.1 Ion range

We already mentioned ion range in Equation 2.15, but what does it represent? The ion range R tells us the total path an ion has travelled inside the solid, but we are mostly interested in how deep from the surface did the ion end. This depth is called projected range, R_p . Its approximate value can be calculated using formula

$$\frac{R}{R_p} \approx 1 + B \frac{M_1}{M_2} \quad (2.18)$$

where M_1 , M_2 are masses of projectile and target atom respectively and B is a slowly varying function of E and R . For a wide range of projectile and target combinations, using the value $B = 1/3$ can serve as good approximation of R_p [4].

The value of R_p is a mean value of depth reached by ions. Scattering processes are uncertain and this uncertainty gives rise to range straggling, the standard deviation from the mean of projected range ΔR_p [4]. Ion range R , projected range R_p and range straggling ΔR_p are shown in Figure 2.4.

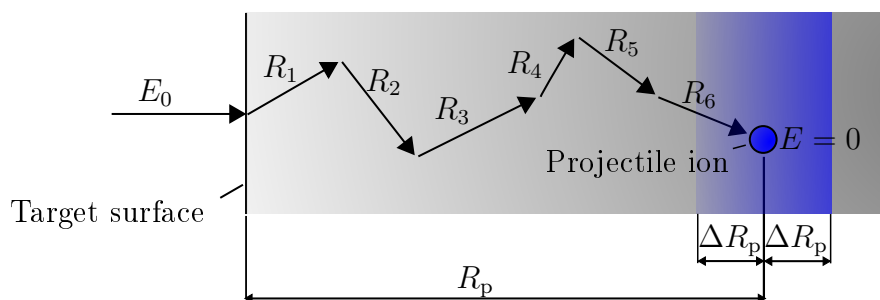


Figure 2.4: Ion range in target material. The total path of ion in solid is given by sum of trajectories between collisions R_i . The mean range of ions measured from surface of solid is projected length R_p and its standard deviation is range straggling ΔR_p .

2.3 Ion irradiation damage

Collision cascades initiated by energetic ions induce damage in irradiated crystalline materials. In the following text we will talk about two main types of damage that occur

in target material, the displacement of atoms induced by energetic ions and changes in crystalline structure caused by energy deposited in material during collision cascades. Both of these processes alter material properties.

2.3.1 Ion induced displacement

Atoms in crystal lattice are held in their positions by binding energy rising from interaction with neighboring atoms. To remove atom from its position in lattice we need to provide displacement energy E_d to overcome the energy holding the atom in place. E_d is dependent on crystallographic directions as shown in Figure 2.5(a). E_d will be high, if we try to displace atom in direction of its closest neighbors in simple cubic lattice. The displacement alongside $[110]$ will require less energy and the displacement in $[111]$ will require minimal E_d . If impinging energetic ion has energy higher than E_d and lower than $2E_d$ in the chosen crystallographic direction, then only one atom will be displaced. The displaced atom will relocate into interstitial position and the impinging ion will settle in created vacancy, see Figure 2.5(b). Impinging ions with energies much higher than E_d will cause a cascade of collisions, where both ions and knocked out atoms will have enough energy to knock out other atoms, giving rise to multiple vacancy and interstitial atom pairs, Frenkel pairs [4]. For ion energies below E_d Frenkel pair won't be created, the knocked atom will return back to its position.

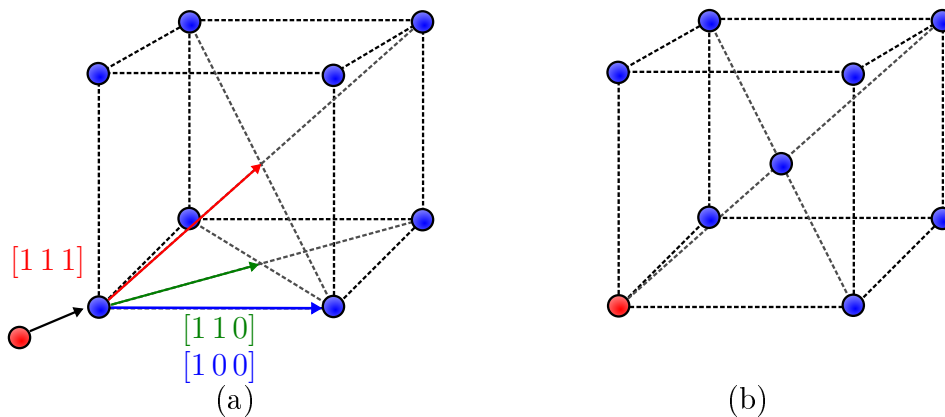


Figure 2.5: Ion induced displacement. (a) A red energetic ion impinges on blue lattice atom. Colored arrows show possible directions of displacement. The movement in $[111]$ direction requires smaller value of E_d than other directions. (b) A displaced atom takes interstitial position in center of cubic lattice. An impinging ion settles in created vacancy.

An energetic ion causes damage along its path travelled in material until it loses all of its energy. The length of this path is given by ion range R . The depth of material modification can be controlled by initial energy of projectile ion as shown in Equation 2.15.

2.3.2 Deposited energy

The primary ion and displaced atoms moving in material deposit part of their energy to lattice atoms alongside their path. This deposited energy can then be distributed between neighboring atoms producing lattice vibrations, heat. It is useful to define deposited energy density θ_D as deposited damage energy $\nu(E)$ per atom per volume V_C , where cascade takes place. θ_D can be approximated as

$$\theta_D \cong \frac{\nu(E)}{N V_C} \quad (2.19)$$

where N is atomic density of target material [4].

If deposited energy density θ_D in a volume of target material reaches energy density of material's melting point θ_{melt} , then the material can melt from the collision cascades happening inside material. Whenever θ_D reaches value of a thermodynamic characteristic of material, the material can undergo structural changes from melting to recrystallization [4]. These effects are dependent on projectile energy E through deposited damage energy $\nu(E)$, allowing us to reach desired material modification using both ion induced displacement and energy deposition by choosing the right energy of impinging ion.

2.4 Applications

The ion irradiation can be used in a variety of material studies to alter various properties of materials. Properties can be modified by ion induced displacement damage and phase transitions induced by deposited energy or by ion implantation process, where impinging ions are implanted inside material to change its properties.

Applications of ion irradiation are many and we will show only a few examples. First examples are various uses of ion irradiation in material modification. Ions can be used to alter structure of material to change magnetic properties [8, 9], optical properties [10] and mechanical properties of irradiated material [11]. Another material modification application realised by us will be presented in chapter 5.

The next field of application is simulation of hazardous environments, where material integrity after irradiation is studied. As an example of hazardous environment a nuclear reactor can be used. Test runs of these reactors are expensive and testing on already operating reactors isn't feasible. Conditions inside reactor can be simulated in vacuum chambers using ion irradiation [12].

3. Irradiation beamline instrumentation

The interaction of ion projectiles with solids has been a research topic for a quite some time and wide variety of ions was used to study and change the properties of an even wider variety of targets. The modification of small targets is possible in most setups using a wide variety of projectiles and energies, but with increasing size of the modified area the number of tools for this type of tasks decreases, especially if desired energies are within the MeV range. These experimental conditions call for a tool dedicated for them.

The irradiation beamline at Uppsala University's Tandem Laboratory is up for this demanding task as it provides the means of sample modification by a MeV ion beams over areas of up to $100 \times 100 \text{ mm}^2$ while being able to store a magazine of up to 20 sample holders inside high vacuum [1]. Photo of irradiation beamline can be seen in Figure 3.1.

This chapter will provide a look at the insides of the beamline and show in detail the entire setup that is able to realize numerous irradiation tasks.

3.1 Accelerator setup

The accelerator setup consists of three main parts: ion injection system, tandem accelerator and beam formation system. In injection system, negative ions of desired species are formed in an ion source, extracted, pre-accelerated towards the tandem accelerator and focused by einzel lens before entering it. Ions are further accelerated inside the tandem accelerator, focused by magnetic quadrupole triplet lens. Following beam formation system is used to select desired energy and charge state by an analyzing magnet. Formed beam is then focused by a magnetic quadrupole doublet lens and sent to irradiation beamline using a switching magnet.

3.1.1 Ion injection system

The tandem accelerator system is equipped with four ion sources to produce a wide variety of beams. A schematic of the ion source system is in Figure 3.2. Sources are labeled as S1 – S4, where S1 and S2 are duoplasmatron ion sources and S3, S4 are Cs sputter ion sources. A beam of negative ions from chosen ion source is selected using injector magnets, dipole magnets and electrostatic deflector. The beam of ions is then

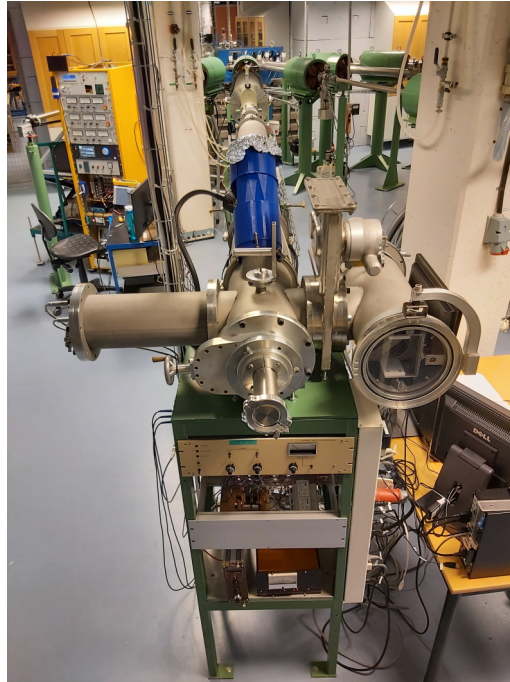


Figure 3.1: Photo of irradiation beamline at Uppsala University's Tandem Laboratory. (Photo by Marcel Janák.)

preaccelerated to desired energy, focused by a pair of einzel lenses and sent towards the accelerator.

The duoplasmatron ion source S1 is used mainly for H, N and O beams. The ion source S2 is dedicated to He. For H, beam currents up to $5\ \mu\text{A}$ can be achieved on the entrance to the accelerator, but a maximum of approximately $2\ \mu\text{A}$ is required for

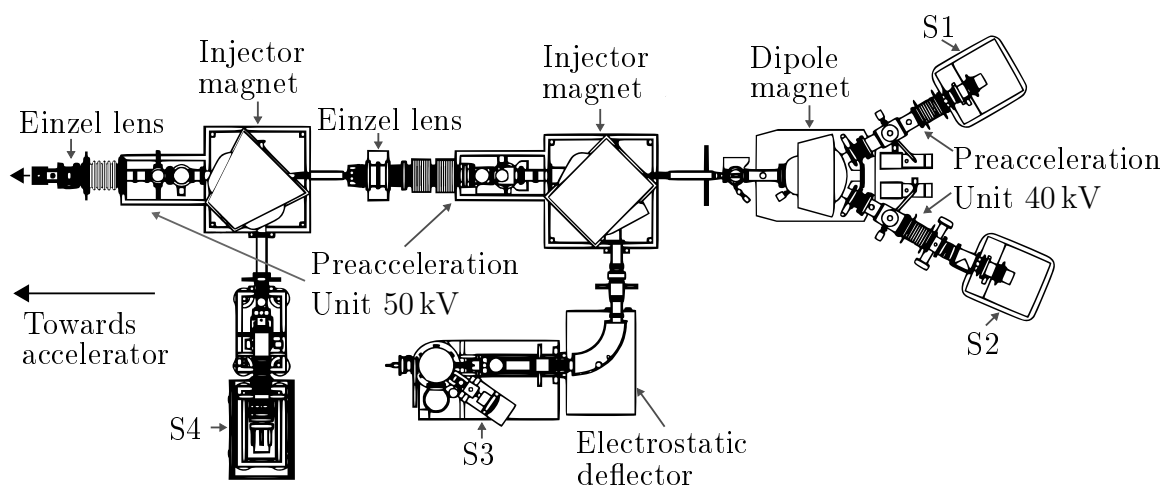


Figure 3.2: Ion injection system schematic. Duoplasmatron ion sources S1, S2 and sputtering ion sources S3, S4 generate negative ions that are preaccelerated and directed towards the tandem accelerator by electrostatic deflectors and injector magnets. The beam is focused by a pair of einzel lenses. (Edited from drawing provided by Jonas Åström.)

accelerator's safe operation. Using He, beams of up to 300 nA can be reached.

Sputtering ion sources S3 and S4 can provide a wide variety of ions available as sputter targets. Available projectiles range from Li to Au with currents of up to 2 μ A depending on the used target. H and O beams can also be realized using hydrate and oxide targets.

3.1.2 Tandem accelerator

The focused beam from the ion source enters the accelerator through x and y steering unit, which allows the beam to be aligned along the accelerator axis. The unit also houses a Faraday cup for measuring the current from ion sources.

A simplified schematic of NEC 5 MV 15SDH-2 Pelletron accelerator can be seen in Figure 3.3. The incoming beam of negative ions is accelerated towards positive high voltage terminal, where the ions are stripped of their electrons using Ar gas atmosphere. High voltage on terminal is realized by a charging chain like in Van de Graaff generator. Created positive ions are then repulsed by high voltage terminal and further accelerated giving ion energy

$$E = (C + 1)V \quad (3.1)$$

where C is the charge state of ion after stripping and V is the terminal voltage [13]. The accelerator is typically operated at maximal terminal voltage of 4.5 MV. Using higher voltages increases chances of discharges in the system causing instability in energy of outgoing ions and eventual damage to the machine. Ions are accelerated in steps by gradient rings. These rings are realising connection between high voltage terminal and ground on both sides of the accelerator. Rings are separated by $G\Omega$ resistors causing the voltage of neighboring rings to slowly drop from the maximal value at terminal to minimal value at ends of accelerator to minimize electric discharges.

Near the accelerator output the beam is focused by a magnetic quadrupole triplet lens and its direction can be modified by y steering unit. The beam continues towards beam formation system.

3.1.3 Beam formation system

The beam of accelerated particles passes through unit containing BPM – Beam Profile Monitor, Faraday cup and x and y slits as shown in Figure 3.4. Particles with desired energy are then selected using analyzing magnet and a series of off-axis Faraday cups can be used for beam normalization. Beam then passes through identical unit with BPM, Faraday cup and x , y slits. Outgoing beam is focused by quadrupole doublet and sent towards chosen beamline using the switching magnet. Beamlines are labeled from T1 to T6, where the irradiation beamline we are interested in is labeled as T5.

Two identical units are used for setting up the beam, x and y slits limit the beam size and by comparing the BPM signals before and after the analyzing magnet the beam can be properly centered and focused. The beam alignment is achieved when the output BPM signal has minimal losses compared to input BPM signal. This means that most of the ions reach the chosen beamline and losses are kept at minimum. The Faraday

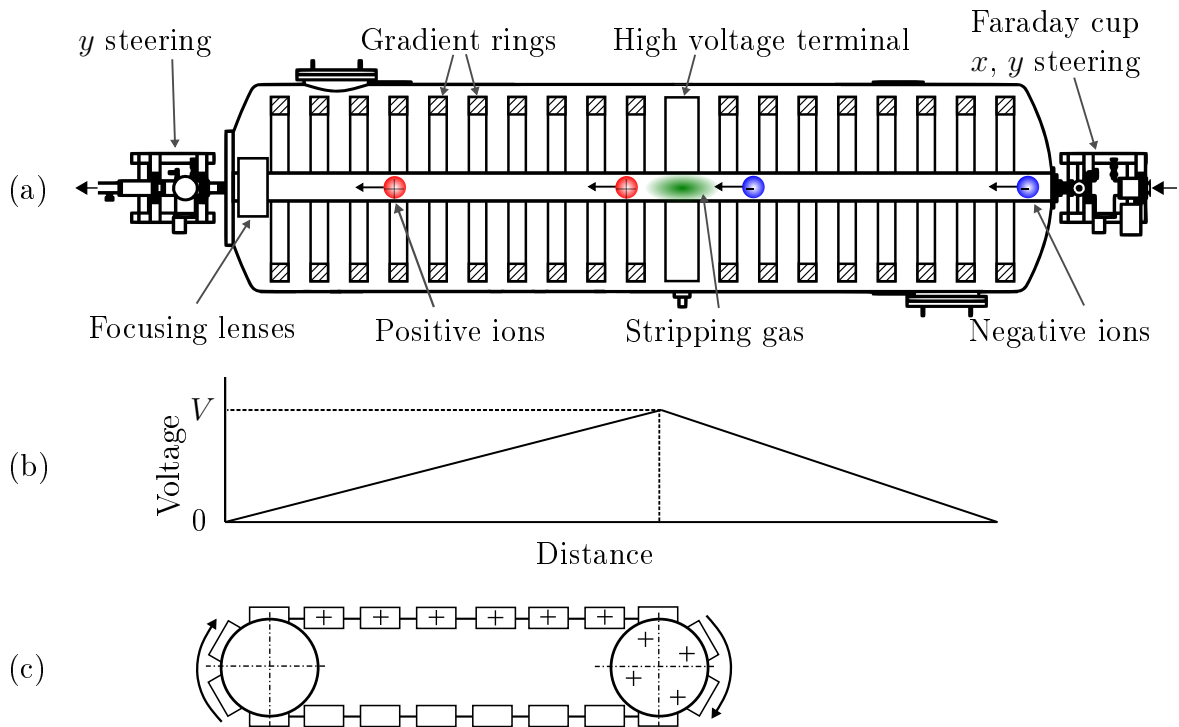


Figure 3.3: NEC 5 MV 15SDH-2 Pelletron accelerator schematic. (a) Cross section of tandem accelerator. Negative ions are injected through steering unit from the right and accelerated towards the high voltage terminal, where they undergo stripping and become positive ions. Positive ions are then accelerated towards the left, focused by magnetic quadrupole triplet lens and pass through another steering unit. (b) The voltage alongside the axis of accelerator. (c) Terminal charging mechanism. The charge is transferred by moving chain towards the high voltage terminal, where it is accumulated. The mechanism is driven by electric motor. (Edited from drawing provided by Jonas Åström.)

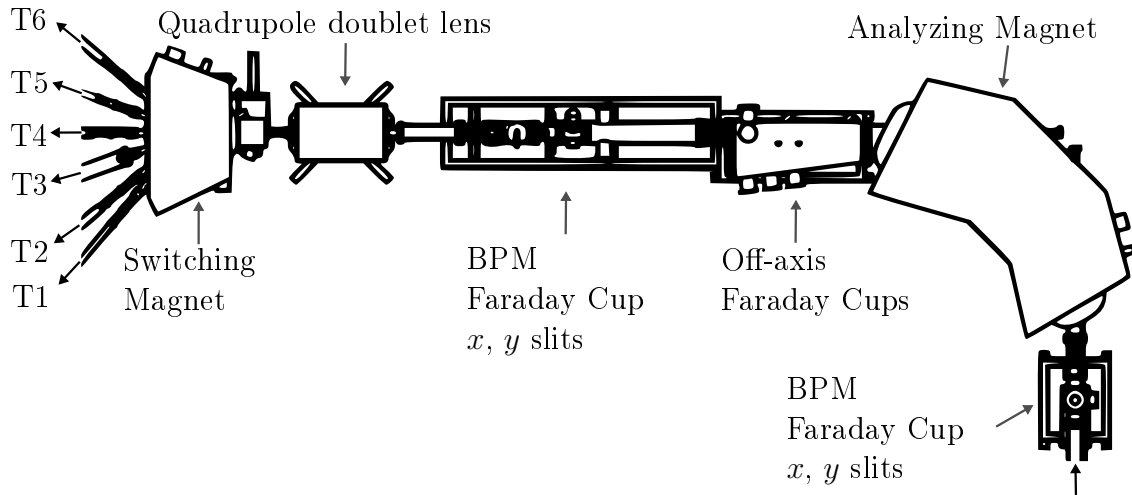


Figure 3.4: Beam formation system schematic. The beam enters from bottom through BPM unit towards analyzing magnet, where ions species and energy is selected. The beam then passes through another BPM unit and is focused by magnetic quadrupole doublet lens and sent towards desired beamline by the switching magnet. (Edited from drawing provided by Jonas Åström.)

cup before the switching magnet is used as a current reference for measurements.

3.2 Irradiation beamline

The beam of MeV ions enters irradiation beamline shown in Figure 3.5 and is first focused by a magnetic quadrupole doublet lens and goes through a deflector unit. The deflector allows the beam to be swept over desired area. The beam is then stopped or allowed to pass through by a beam stop towards the main chamber, where samples are irradiated by incoming beam and where irradiation parameters can be measured and adjusted accordingly to experimental needs. The main chamber also houses the sample transfer system, which will be described in detail in chapter 4.

3.2.1 Deflection unit

The focused beam from magnetic quadrupole lens is swept over the sample area using vertical and horizontal electrostatic deflector units as shown in Figure 3.6(b). A schematic of a horizontal unit can be seen in Figure 3.6(a). Two apertures with adjustable field clamps are interconnected with mounting rods forming the body of deflector. Mounting rings with connector plates are attached to aforementioned rods. Deflector plates are mounted on insulating elements and attached to connector plates to insulate the deflector plates from rest of the assembly. The vertical unit is realized in a same way.

The voltage difference between deflector plates is realized by triangular wave generators operating at frequencies of 517 Hz and 64 Hz for vertical and horizontal deflection respectively and output from -10 kV to $+10$ kV, giving a peak to peak maximum volt-

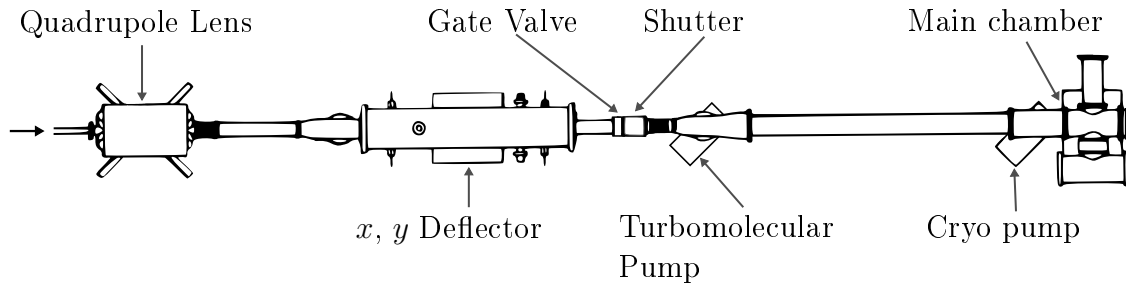


Figure 3.5: Irradiation beamline schematic. The beam entering from the left is focused by magnetic quadrupole doublet lens and swept over sample located in main chamber using deflector unit. The beam can be stopped using the shutter. The gate valve can be closed to keep vacuum on the left side intact and allow for venting of the right side only. (Edited from drawing provided by Jonas Åström.)

age of 20 kV. The voltage amplitude can be set separately for x and y direction using potentiometers and each of them can be turned on and off at will. This allows samples of up to $100 \times 100 \text{ mm}^2$ to be irradiated. The frequency ratio is locked and provides optimal dose uniformity [1, 14].

3.2.2 Shutter

To start and stop the irradiation of a sample, a shutter is used. It's formed by a stainless steel plate that blocks incoming ions as shown in Figure 3.7(a). Shutter movement is realized by a magnetic force. The force is provided by current controlled electromagnet. When the current is running, the shutter is in open state as in Figure 3.7(b). Without current, the shutter is closed. This serves as a safety measure in case of power supply malfunction.

3.2.3 Main chamber

The main chamber consists of two subchambers separated by a gate valve as shown in Figure 3.8. Magazine chamber houses samples mounted in magazine and serves as a load-lock for sample loading. Pirani gauge measures pressure in magazine chamber during rough pumping from atmosphere, when the pressure is deemed sufficiently low by the beamline user, the gate valve towards irradiation chamber can be opened.

This chamber contains shuttle that together with magazine forms the sample transfer system that will be discussed in chapter 4. Samples transferred here are irradiated by swept beam. Samples inside irradiation chamber can be observed through viewport using camera. The beam current and irradiation homogeneity can be measured using Faraday cup array with adjustable vertical position consisting of three separate cups. Faraday cups are on line 5 centimeters apart as shown in Figure 3.9. All three cups have area of 1 cm^2 . Central cup can be used as current reference for unswept beam. For swept beams it can be used in combination with Faraday cup before switching magnet at entry of irradiation beamline to calculate irradiated area. This will be discussed in chapter 4. Pressure in irradiation chamber is monitored by Pirani gauge and cold

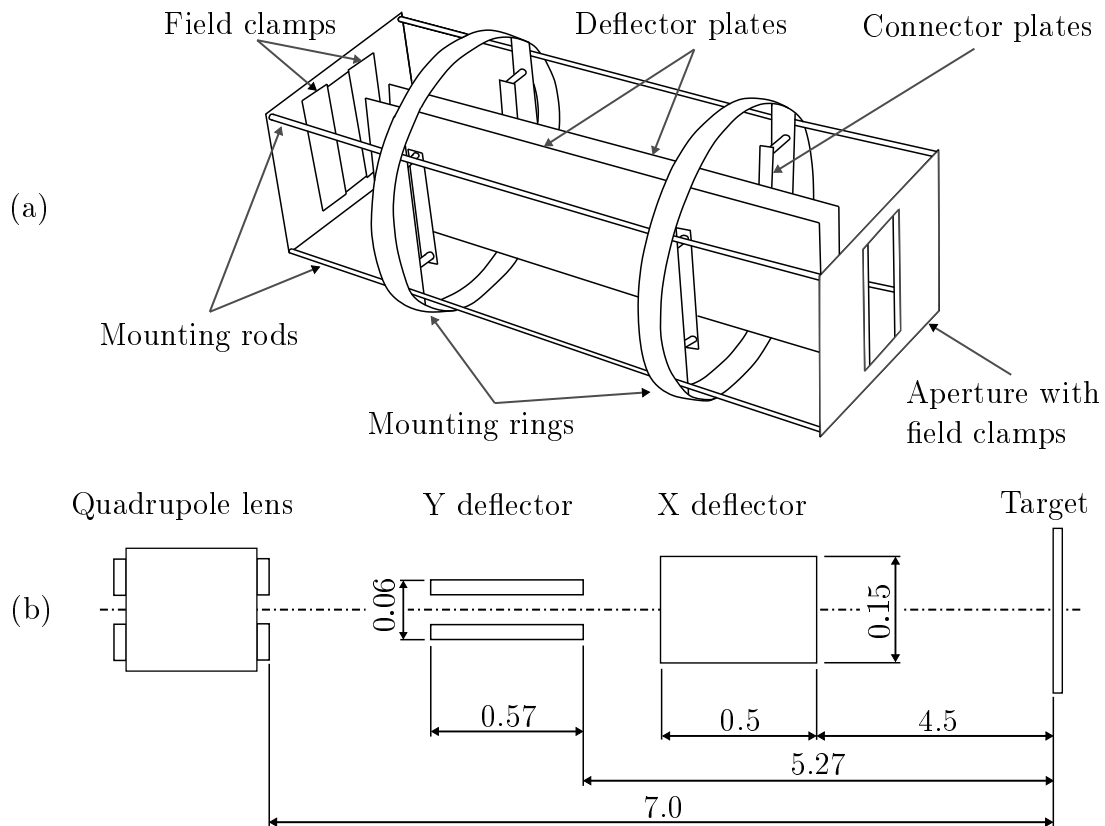


Figure 3.6: Deflector unit schematic. (a) Schematic of horizontal deflector. Two apertures with adjustable field clamps are interconnected by mounting rods. Mounting rings mounted on rods are then used to achieve non-conductive connection of deflector plates with connector plates attached to mounting rings. (Edited from photo in [1].) (b) Deflector unit dimensions. Dimensions are in meters and taken from [1].

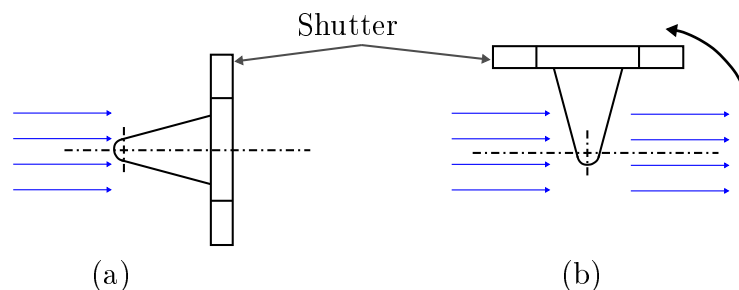


Figure 3.7: Shutter schematic. (a) The shutter blocks the incoming beam depicted as blue arrows, beam off state. (b) When the driving current is switched on, the shutter rotates 90° anticlockwise to allow the incoming beam to pass, beam on state.

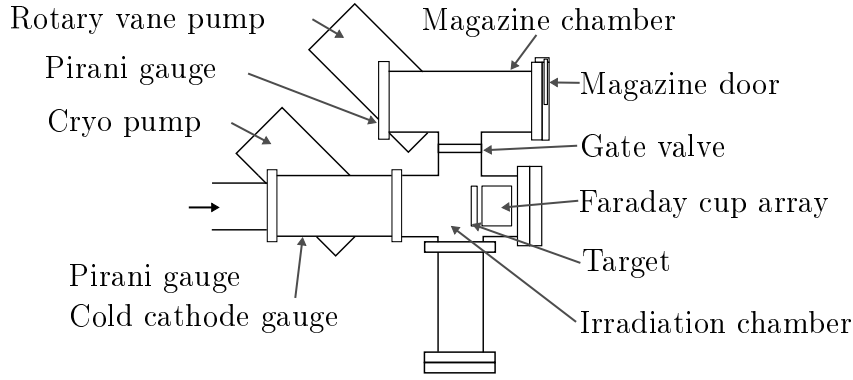


Figure 3.8: Main chamber schematic.

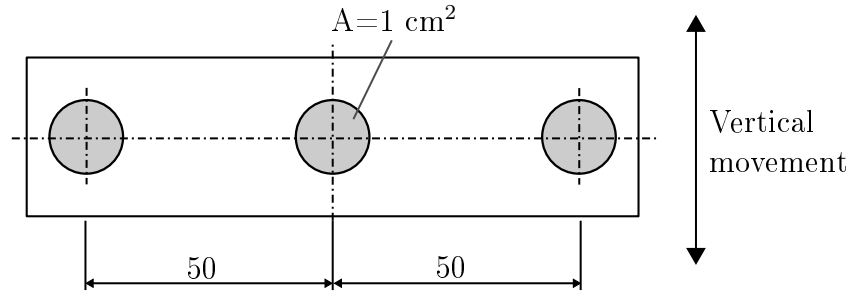


Figure 3.9: Faraday cup array schematic. Array is allowed to move vertically to check homogeneity of entire irradiated area. Dimensions in millimeters.

cathode gauge.

3.2.4 Chamber vacuum

The high vacuum (HV) inside irradiation beamline is realized by four pumps. In Figure 3.5 two of these pumps and their position along the beam path can be seen. The rough vacuum is realized by two-stage oil sealed rotary vane pump connected to magazine chamber visible in Figure 3.8. Pressure of down to $2 \cdot 10^{-2}$ mbar can be reached using this pump. The HV is reached by turbopump backed by the same type of rotary vane pump. Pressure of $3 \cdot 10^{-6}$ mbar can be reached using only the turbopump. To reach even better vacuum, cryopump is used. A combination of cryopump and turbopump can reach pressure of $1 \cdot 10^{-6}$ mbar during experiments.

Pressure in the chamber is measured in two spots, at magazine chamber and near the cryo pump. The magazine chamber is equipped with a Pirani gauge to observe rough pumping status of the load-lock chamber. When pressure is deemed sufficiently low by the beamline user, the gate valve can be opened. Pressure in irradiation chamber is measured by a combination of Pirani gauge and cold cathode gauge to cover entire region from low vacuum to HV.

4. Sample transfer system: Modifications and improvements

The irradiation beamline at Uppsala University was first presented in 1989 in paper by Hallén et al. [1]. It was remotely controlled from a computer and boasted a sample transfer system with magazine for 20 sample holders allowing for automatic batch irradiation applications. The samples transfer system was driven by two stepper motors controlled by microprocessors. The heart of the system was I/O (input/output) board realizing communication between the computer, microprocessors, shutter and sensors inside the main chamber. The entire setup was controlled by computer application written in Turbo Pascal language and contained safety measures for leaks in the vacuum system, power outages and user error to prevent damage to system components.

Another modification came in 1996. The stepper motors were replaced by brushless DC (direct current) motors and I/O board was substituted by a programmable logic controller, PLC. The PLC connection to PC was realized by PCI Express card communicating via 16 bit libraries and application written in LabView [2]. The PLC was plugged to printed circuit board, PCB, that realized processing of all input and output signals and control of all main chamber components. The DC motors made the sample transfer faster and smoother thanks to a cleverly designed circuitry. Many safety sensors were added to system to further ease work with the system for new users. The operating system used on the PC was Windows 1995.

The present modification came in 2020. Goal of this modification was replacement of old control PC running Windows 1995 operating system, OS, with a modern machine. This simple task turned into a large project. Modern systems are unable to use 16 bit libraries used for communication with provided PLC, unless an older OS is emulated on it. This problem could be solved in two ways, the aforementioned OS emulation or design of a new control unit to replace the PLC and realize all signal processing and controls. We decided to go for the second option to allow for easier modifications in the future.

The system unmodified since 1996 was consequently taken apart, studied and improved. Mechanical parts of sample transfer system were optimised to minimise misalignments and accidental dropping of samples in vacuum, the downsides of the old system. The PLC and its PCB were replaced by a simple control unit connected to PC using data acquisition card, DAC, from National Instruments connected to computer via USB connector. The PCB design was based on the original circuit with modifications to achieve compatibility with the rest of the system and DAC. The original

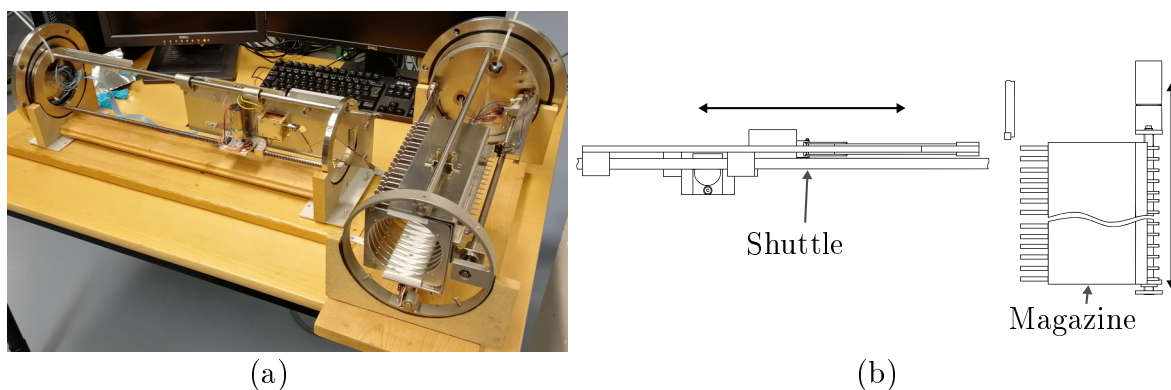


Figure 4.1: Sample transfer system. (a) Photo of sample transfer system taken out of the main chamber before mechanical modifications. Left part of the system is the shuttle, right part is the magazine. (b) Sample transfer system schematic showing its two main parts, shuttle and magazine. The movement directions of each part are indicated by arrows next to them.

application written in LabView was replaced by a new improved version using the same language.

The following text will present the sample transfer system in its current state after the modification in 2020. Modifications, improvements and replacements to the setup alongside new control application and all of its features will be shown and described. The first experimental application of upgraded system will then be shown in chapter 5.

4.1 Sample transfer system

Transportation of samples from magazine chamber to irradiation chamber is realized by a sample transfer system shown in Figure 4.1. The system is formed by two parts, shuttle and magazine. The shuttle transfers the samples between the two chambers and the magazine aligns the desired sample to allow its transfer using the shuttle. These two building elements will be described in detail in the following text alongside basic constructions of sample holders.

4.1.1 Sample holders

Before we fully dive into shuttle a magazine working principles, sample holders will be mentioned. Sample holders for irradiation beamline come in many shapes to allow mounting of various samples. The basis of all holder designs is a square with side length of 11 cm and a pin slot on upper side to allow the holder to be grabbed by the shuttle. Rest of the holder shape depends on what samples are to be mounted on it. Two of the holder designs can be seen in Figure 4.2.

A 4 inch wafer sample holder can be seen in Figure 4.2(a). Wafers of 4 inches in diameter are inserted into a slot and locked in place using screws with teflon washers. These holders are made of aluminium plates to make them light and reduce load on shuttle mechanism. A drawing of this holder can be seen in attachment SH-4I.

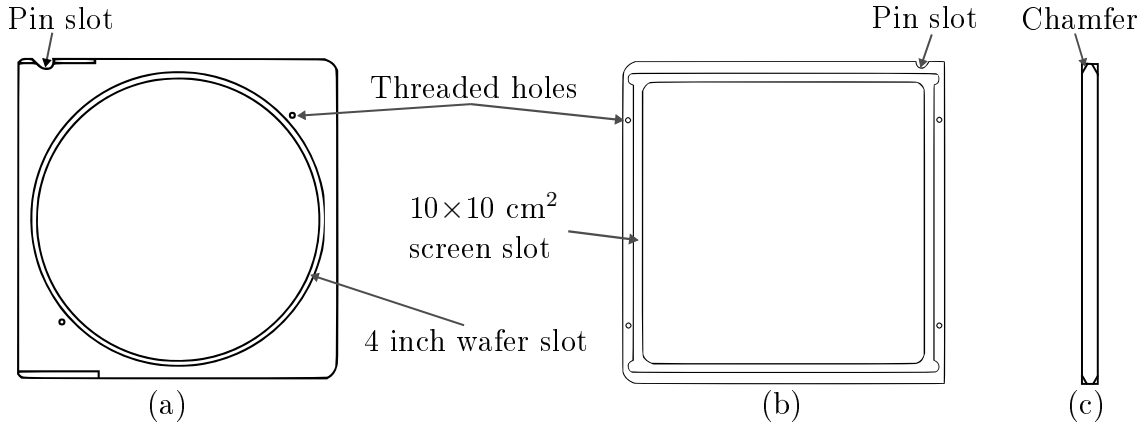


Figure 4.2: Sample holder schematics. (a) Sample holder for 4 inch wafer mounting. Wafers are inserted into a slot and secured with mounting screws inserted in threaded holes. (b) Fluorescent screen holder. Mounting is realised the same way as for wafers. (c) Left view on sample holder in subfigure (a). Holders are chamfered in places where they are grabbed by a shuttle grip for improved alignment.

The second holder shown desing in Figure 4.2(b) is a holder of a fluorescent screen. The fluorescent screen is mounted in a screen slot and held in place using screws with steel washers. This holder design is made of stainless steel to maintain its rigidity and minimise bending. Fluorescent screens produce light when hit by ions and are used to align the beam and see the area irradiated by swept beam at irradiation beamline. A drawing of a screen holder is in attachment SH-FS.

4.1.2 Shuttle

The transportation of samples between magazine and chamber is realized by the shuttle, whose schematic is shown in Figure 4.3. The shuttle is mounted on two rods using plain bearings. The top rod is polished, while the bottom rod is a rack for DC motor's pinion. The movement is realised by Escap 26L28 216 12V DC motor with K27 2R 17 gearbox whose transfer ratio is 55.7:1.

The position of the shuttle is measured by a pair of potentiometers connected by tension springs as shown in Figure 4.4, and both extreme positions the shuttle can reach contain safety switches that turn off the power to the motor in current movement direction if pressed. These prevent damage to the motor by a stall current. The potentiometer resistance during movement is changed by contact with one of the two pins. The first one measures position inside main chamber, the second one inside the load lock. The position between irradiation chamber and load lock is a constant number and actual position in this region is unknown as it is not needed for system operation.

In order to transfer samples, the shuttle needs to grab them, this is realized by the grip mechanism, which can be seen in Figure 4.5. Contact with the sample is achieved by a Sodemann E03600341500S [15] tension spring pulling the grip jaws against each other. Opening of the grip is possible thanks to a Kuhnke H6206-F 24V solenoid actuator [16]. Upon magnet activation, the grip plates are moved towards the electromagnet

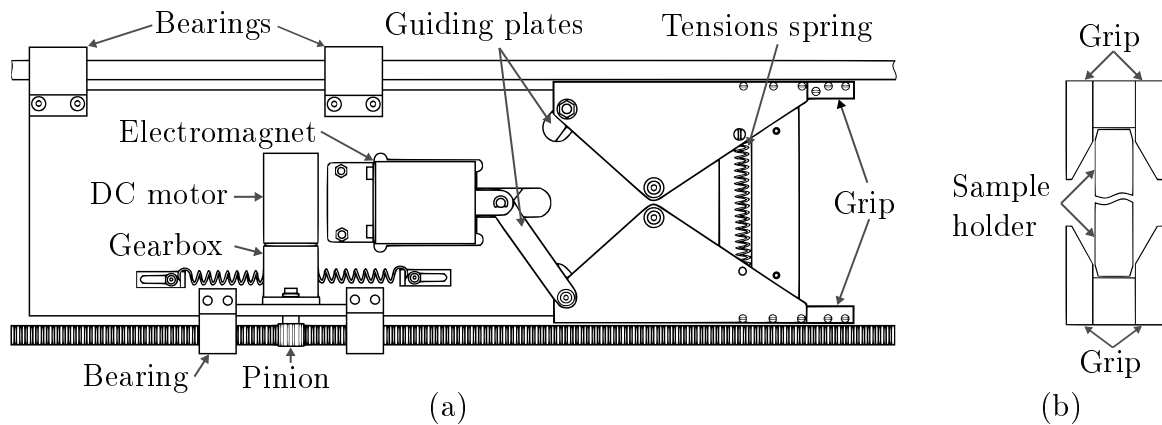


Figure 4.3: Shuttle schematic. (a) Front view of the shuttle depicting its main components. (b) Right view of subfigure (a) showing detail of a sample holder grasped by the shuttle’s grip mechanism. Chamfers on both the grip and sample holder help with alignment during the sample holder grabbing process.

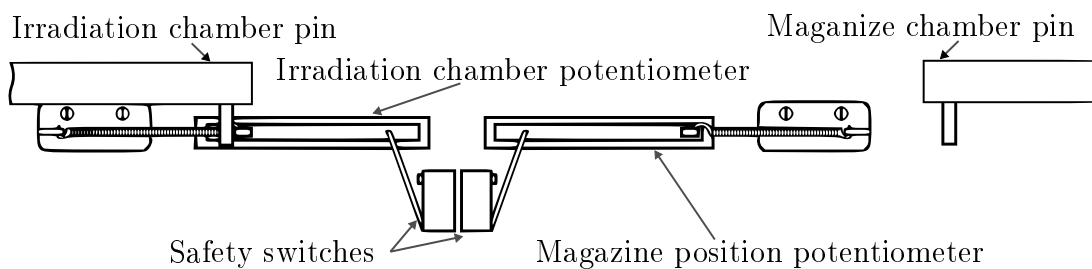


Figure 4.4: Potentiometer system schematic. When the shuttle moves left, the irradiation chamber pin comes into contact with the irradiation position potentiometer and changes its resistance. If it moves too far left, the safety switch will be pressed. This will forbid any movement towards the left and shuttle can only be moved right, towards the magazine chamber. The same system is used on magazine chamber side.

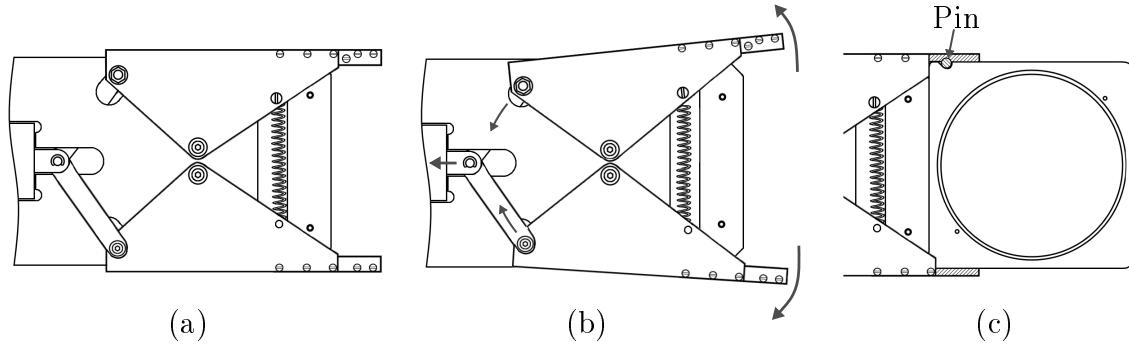


Figure 4.5: Grip schematic. (a) Closed grip. (b) Grip opened by active solenoid actuator. (c) Grip holding a sample holder. The circular pin in a slot restricts sample holder's movement.

and grip is opened, because the electromagnet force prevails over the force created by tension springs Figure 4.5(b). When the electromagnet is turned off, the grip is closed by the tension spring force Figure 4.5(a). The sample movement during transport is restricted by a pin in top jaw as seen in Figure 4.5(c). The sample grabbing procedure will be described in subsection 4.4.1.

4.1.3 Magazine

In order to run irradiations continuously without the need to open the load lock after every irradiated sample, a magazine able to house up to twenty sample holders is used. Sample holders are mounted onto cassette shown in Figure 4.6. A stainless steel body is equipped with teflon slots to minimise friction and reduce vibrations during sample transfer. Up to twenty sample holders with sample area of up to (10×10) cm² can be mounted. When all samples are mounted, the cassette is inserted into the magazine body and fastened in position by a butterfly nut.

The magazine body, shown in Figure 4.7 is mounted on two guiding rods and held in right position using polished stainless-steel cylinders on plain bearings to minimise friction. The movement of the magazine body is realized by an Escap 26L28 216 12V DC motor using a K27 2R 17 gearbox with transfer ratio of 55.7:1, the same model as used in the shuttle. A threaded rod is rotated by the motor and causes linear motion of the magazine body by contact with threaded brass ring affixed to the magazine body. The precise positioning of the magazine with respect to shuttle is possible thanks to a GP1S094HCZ0F photo interrupter triggered by position rods, that make the sample holders stop directly in front of the shuttle allowing for a proper grabbing. A calibration of first position is realized by a **Home** switch triggered by a contact with magazine, which also acts as a safety measure to prevent the magazine from colliding with load lock walls. When the switch is triggered, the magazine starts to move in opposite direction and stops in first position after corresponding rod passes through and triggers the photo interrupter. For safety of operation an GP2L01F reflective photo interrupter is used to prevent movement of magazine while the shuttle is holding a sample holder still located inside teflon slots. The other side of the load lock chamber is equipped

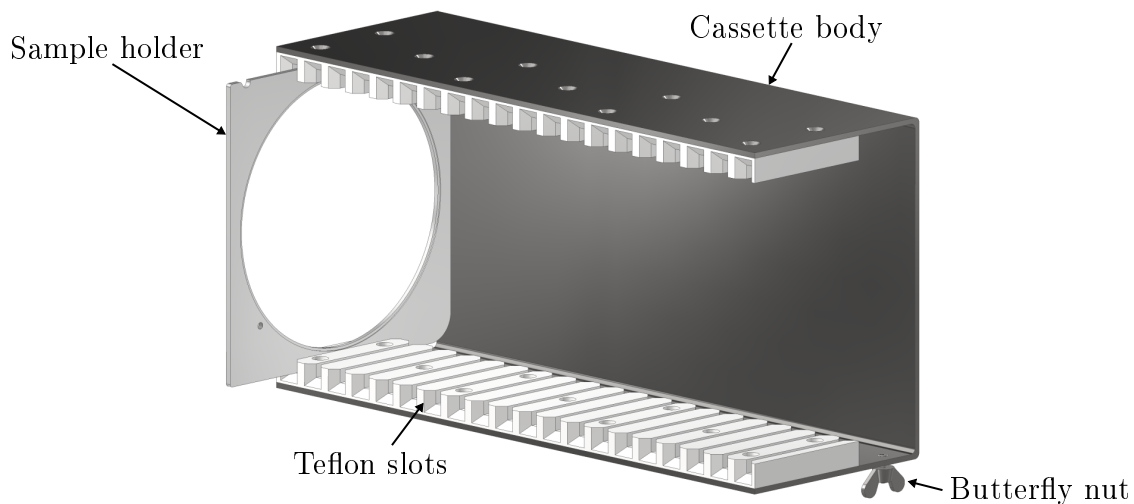


Figure 4.6: 3D image of cassette. Teflon slots are mounted onto cassette body and up to 20 sample holders can be held at the same time. The loaded cassette is then inserted in magazine and fastened using a butterfly nut. Multiple cassettes are available allowing for a fast switching of samples in the load lock.

with **End** switch to prevent collisions similar to the **Home** switch.

4.2 Grip improvements

One of the most notable flaws of the original system was sample transfer reliability. The shuttle's grip mechanism allowed tilting of the gripped sample holder frames as shown in Figure 4.8(a), which was unwanted. Such movements often led to accidental dropping of samples during transfer and misalignments between shuttle and magazine, which made returning of sample holders to cassette slots nearly impossible. These problems were solved by modification of shuttle's grip mechanism as shown schematically in Figure 4.8(b) and in detail in attachments GRIP-AS-1 and GRIP-AS-2. Following text will describe the assembly depicted in mentioned attachments.

The first step was design of new grip plates to maintain compatibility with rest of the system. Grip plates were designed in two pairs, grip plates A with counter sunk clearance holes for M2 screws and grip plates B with threaded holes for easy assembly, see attachment GRIP-PL. To each pair of grip plates a grip body is attached and grip jaws are then mounted upon it. Top body and jaws differ from the ones at the bottom by addition of a pin to hold the sample holders in place, see attachments GRIP-GB and GRIP-GJ. The increased contact length L and depth H shown in Figure 4.8(b) improve rigidity of the system and minimise unwanted sample holder movement.

The tension spring from the old grip was measured and an optimal replacement was found in Sodemann E03600341500S tension springs [15]. The new spring provides more force compared to original design, which led to modification of the guiding plates, see attachment GRIP-GP, to increase the initial force of the solenoid actuator. These modifications increased grip opening and closing force and speed allowing for faster

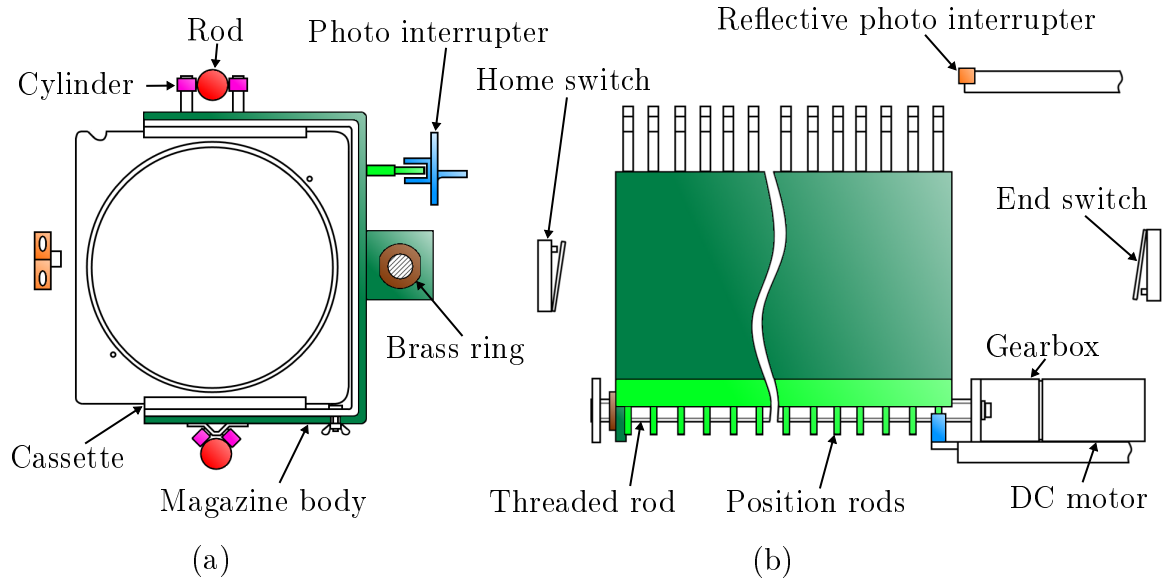


Figure 4.7: Magazine schematic. (a) Front view of magazine with cassette inserted. (b) Top view of magazine with the cassette inserted rotated 90° clockwise. Part colors are shared between the subfigures.

and more firm grip of sample holders.

4.3 Control unit replacement

The next step of the beamline modernisation was replacement of a control unit to achieve compatibility of the transfer system with modern computer and operating system, OS. To do so, the programmable logic controller, PLC, the printed circuit board, PCB, and the PCI card shown in Figure 4.9 had to be replaced [17]. The NI USB-6001 data acquisition card [18], DAC [17], from National Instruments was chosen as a replacement for the PCI card. Since the system was controlled by a LabView program from the same company, compatibility was assured. The PLC and PCB replacement was slightly more complicated. A new PCB had to be designed to make it compatible with the new DAC. The design of such PCB will be presented in the following text.

The finished design of the PCB can be split into two main parts shown in attachments CONBO-PL-1 and CONBO-PL-2. Circuit parts in the dashed rectangles are components of the irradiation beamline connected to the PCB board. Each connection between the PCB and the system part is labeled by an alphanumeric combination, where letter denotes subcircuit. The PCB board also provides connection with the USB DAC, which provides inputs and outputs shown in the drawings as variable names with arrows below them coming in and out of the circuit respectively. Power to the circuit is provided by Comatek PSC 24V DC and Comatek PSC 12V DC power supplies [19, 20].

We will begin with the first attachment mentioned and describe parts of the circuit. The CONBO-PL-1 drawing consists of three separate subcircuits: shutter control circuit, shuttle position measurement circuit and shuttle movement circuit. Then we

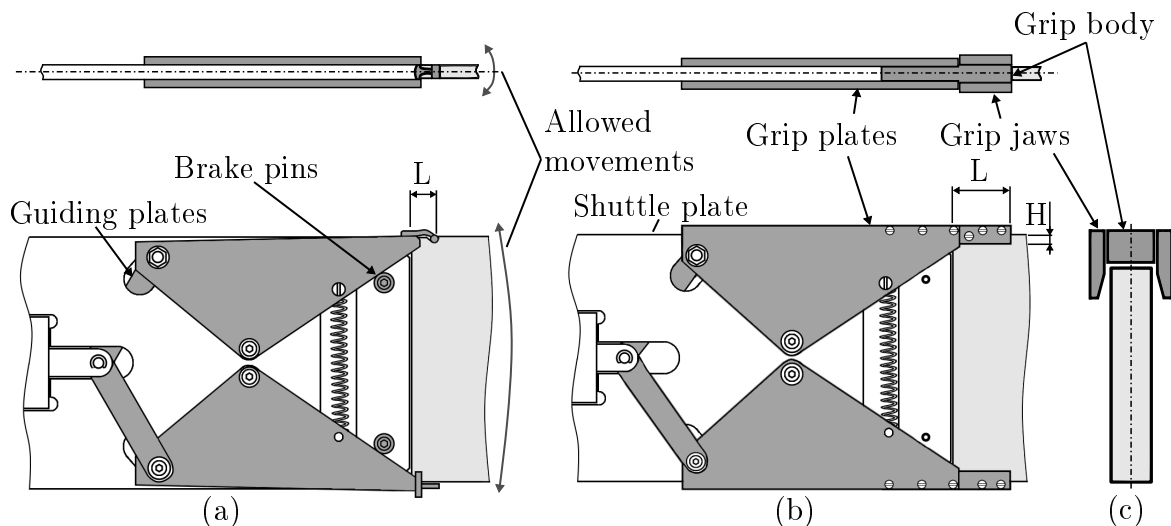


Figure 4.8: Grip improvements schematic. Sample holder (light grey) is held by the grip in all subfigures. (a) Top view and front view of the old grip mechanism. Grey parts were replaced. The stopping of closing movement was realised by braking pins. (b) Top and front view of modified grip mechanism. The improved rigidity of the mechanism removed undesired movements allowed by previous design. Grey parts were newly installed. Braking pins are no longer needed. The closing motion is stopped by the shuttle plate's edge. (c) Side view of modified grip. The sample holder is stationary while held by the grip. Chamfers on the grip jaws help with alignment during the holder grabbing process.

will move on to attachment CONBO-PL-2, where magazine movement circuit, sensor circuit and grip control are shown.

4.3.1 Shutter control

To start and stop the irradiation process, a shutter is used. The control of the shutter is realised by a remotely controlled DC power supply unit, PSU, as shown in Figure 4.10. The DAC card generates a transistor-transistor logic, TTL [17], signal **Beam stop**. TTL signal is high when **Beam stop** is true, logical one in Boolean logic [17], and power supply is remotely switched on, opening the shutter and allowing the beam to pass. When the **Beam stop** is low, the power supply is switched off and the beam is blocked.

4.3.2 Shuttle position measurement

The position of the shuttle is measured by two potentiometers as was mentioned in chapter 3. The entire position measurement circuit can be seen in Figure 4.11. 24 V from DC power supply's positive rail are reduced by a 10 V Zener diode to power a AD584JNZ precision voltage reference [21]. The voltage reference outputs a 10 V with 3 % accuracy and 10 mA output current. A 1 μ F capacitor is used to minimise the current spike when the voltage reference powers up to prevent damage to components. Next up is a GL324 operational amplifier [22] used as a voltage follower. Voltage

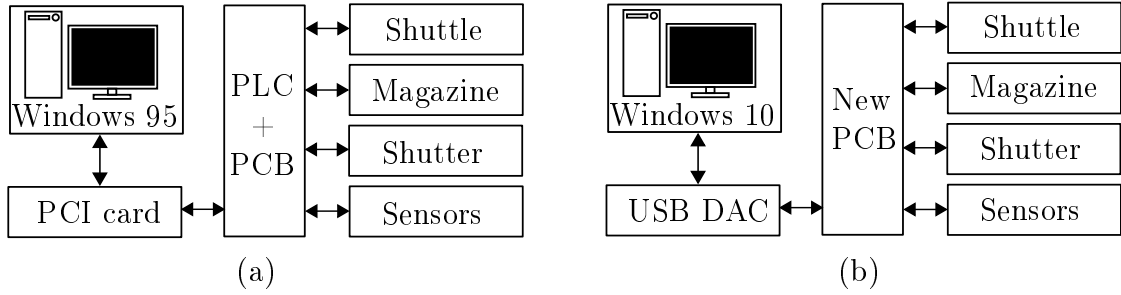


Figure 4.9: Control unit schematic. (a) Original control unit. The communication between PC and system was realised by PCI card, PLC and PCB. (b) New control unit. The PCI card was replaced by an USB DAC. The PLC and the PCB were replaced by a single new PCB. The OS was upgraded to a more recent version.

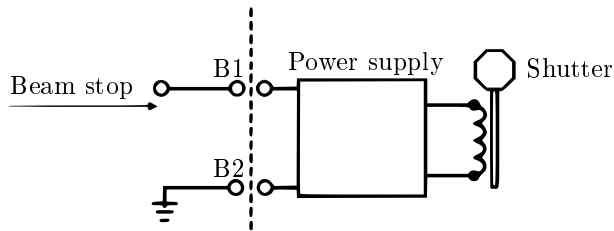


Figure 4.10: Shutter control circuit diagram. The PCB board is on the left of the dashed line.

followers provide a unity voltage gain and serve as an isolator to minimise current in the following circuit[17].

After the voltage follower is first of the two 1 k Ω trimmer potentiometers set at 500 Ω . These are used for calibration of position values provided by two linear potentiometers. The first potentiometer measures the shuttle position in irradiation chamber, the target potentiometer, while the second potentiometer measures the position in magazine chamber, the sample potentiometer. Both of these potentiometers have resistance range from 2 Ω to 10 k Ω . The voltage is measured on the two linear potentiometers connected through another voltage follower to a DAC input labeled as **Shuttle position**, which is continuously read by the control software.

4.3.3 Shuttle movement

The shuttle movement is realised by a 12 V DC motor powered by a 12 V PSU. A HF46F power relay [23] is used to switch on and off the current to the motor. The relay's on state is controlled by an IRLZ14 MOSFET [24] switch circuit. When **Shuttle on/off** input signal is high, the transistor switches to open state and relay switches to on state. When the signal is low, the relay switches to off state. MOSFET is separated from the DAC by a 100 Ω resistor to minimise current flowing to DAC to protect its delicate circuitry from current induced damage. A 10 k Ω resistor connects transistor to ground to provide zero voltage at the transistor's gate in case of DAC malfunction.

The motor power is regulated using a DAC generated pulse width modulation, PMW [17]. The PMW is realised by switching the transistor on and off to reach the

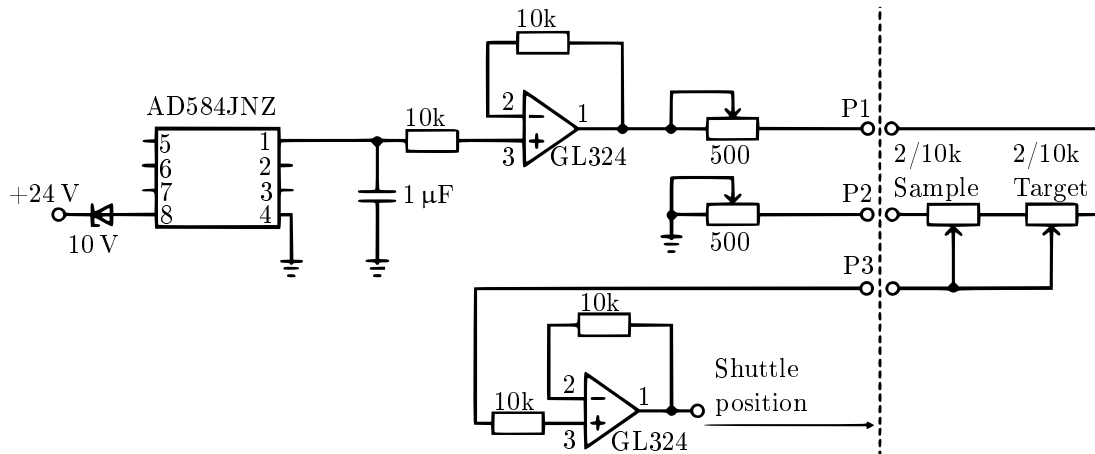


Figure 4.11: Shuttle position measurement circuit diagram. The PCB board is on the left of the dashed line.

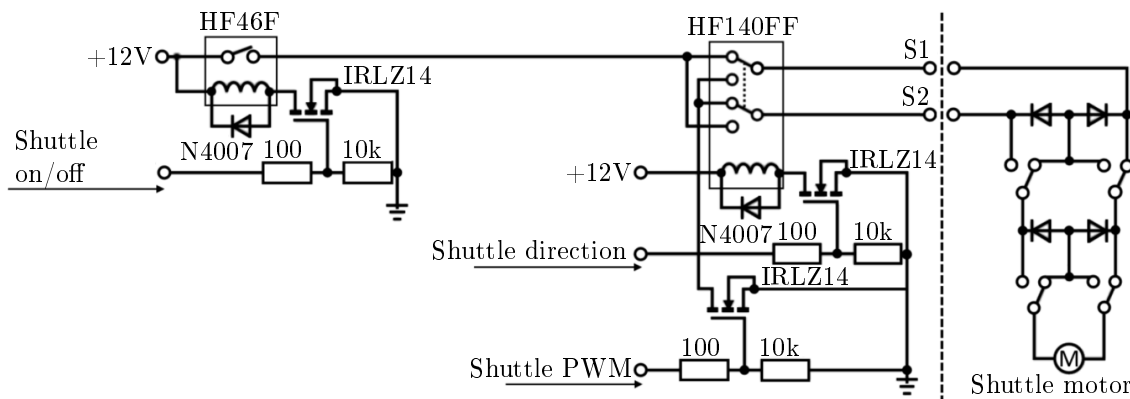


Figure 4.12: Shuttle movement circuit diagram. The PCB board is on the left of the dashed line.

desired percentage of power input. To achieve 70% power the MOSFET has to open for 70% of the time and closed for the remaining 30%. In our case the PMW is used to limit maximal speed of the shuttle for safe sample transfer.

The direction of the shuttle movement is realised by a HF140FF power relay [25] controlled by an IRLZ14 MOSFET switch circuit. When the **Shuttle direction** input signal is high, the shuttle moves in one direction. When the signal is low, the current flow through the motor changes direction and shuttle moves in the other direction. Both relays are protected from solenoid voltage spikes by N4007 flyback diode [26, 17].

The shuttle movement is protected by two safety switches to prevent collisions and thus damage to the system. These switches limit movement range to prevent collision of shuttle and magazine on magazine chamber movement end point and on the other end of the shuttle's path to prevent damage to cables and vacuum feedthroughs. The working principle of the switches was described in subsection 4.1.2.

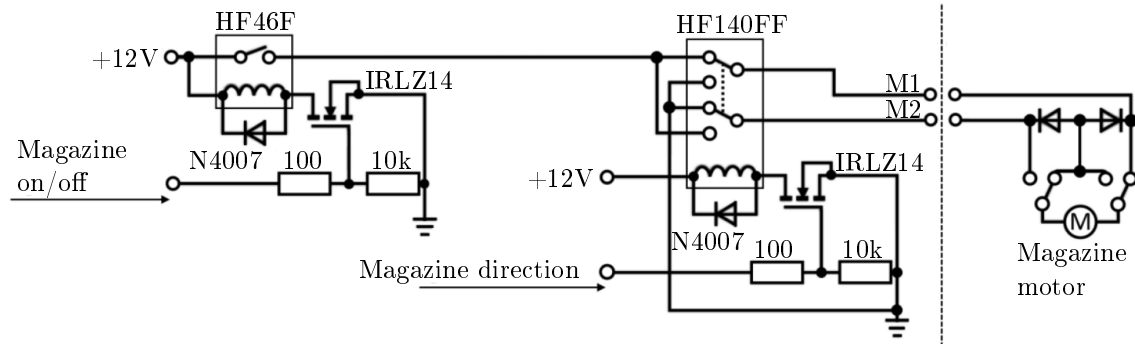


Figure 4.13: Magazine movement circuit diagram. The PCB board is on the left of the dashed line.

4.3.4 Magazine movement

The movement of the magazine is realised almost in the same way as the movement of the shuttle. The first difference are the names of the power switch input, **Magazine on/off**, and direction changing input, **Magazine direction**. Second difference are safety switches. Instead of using mechanical switches connected directly to the motor circuit like the shuttle, magazine switches are read using the DAC and processed by the control software to stop the movement. These switches, named **Home** and **End**, will be further described in the next subsection and in subsection 4.4.2.

4.3.5 Sensor circuit

As it was already mentioned, the irradiation beamline uses many switches and sensors to realise its precise positioning while maintaining safety during the sample transport. The sensor circuit can be seen in Figure 4.14. A 24V DC voltage is reduced using a voltage divider combined with a voltage follower. The high impedance of the follower allows us to use unloaded voltage divider formula to calculate the required resistors [17]. A combination of 1 k Ω and 4.3 k Ω resistors was chosen to provide an output voltage of 4.52 V and minimal current to meet the input requirements of the DAC allowing voltages of up to 5 V to be connected. The reduced voltage is then applied to all of the sensors.

The first group of sensors are contact switches. When an external force is applied, the switch circuit get's closed and high value is detected by DAC. **Valve status** switch gives a high value when the gate valve connecting the magazine chamber and the irradiation chamber is opened, preventing shuttle collisions with gate valve by restricting power to the shuttle. The other two switches are located in magazine chamber and are labeled **Home** and **End**. The **End** switch prevents collisions of magazine with the far end wall of the magazine chamber and preventing damage to the cables and stall current damage to the DC motor. The **Home** switch provides the same safety limits, but it's also used for magazine position calibration, which will be discussed in subsection 4.4.2.

The second group of sensors uses photo interrupters whose outputs are read using pull-up resistors. A photo interrupters emit light using a a light emitting diode, LED,

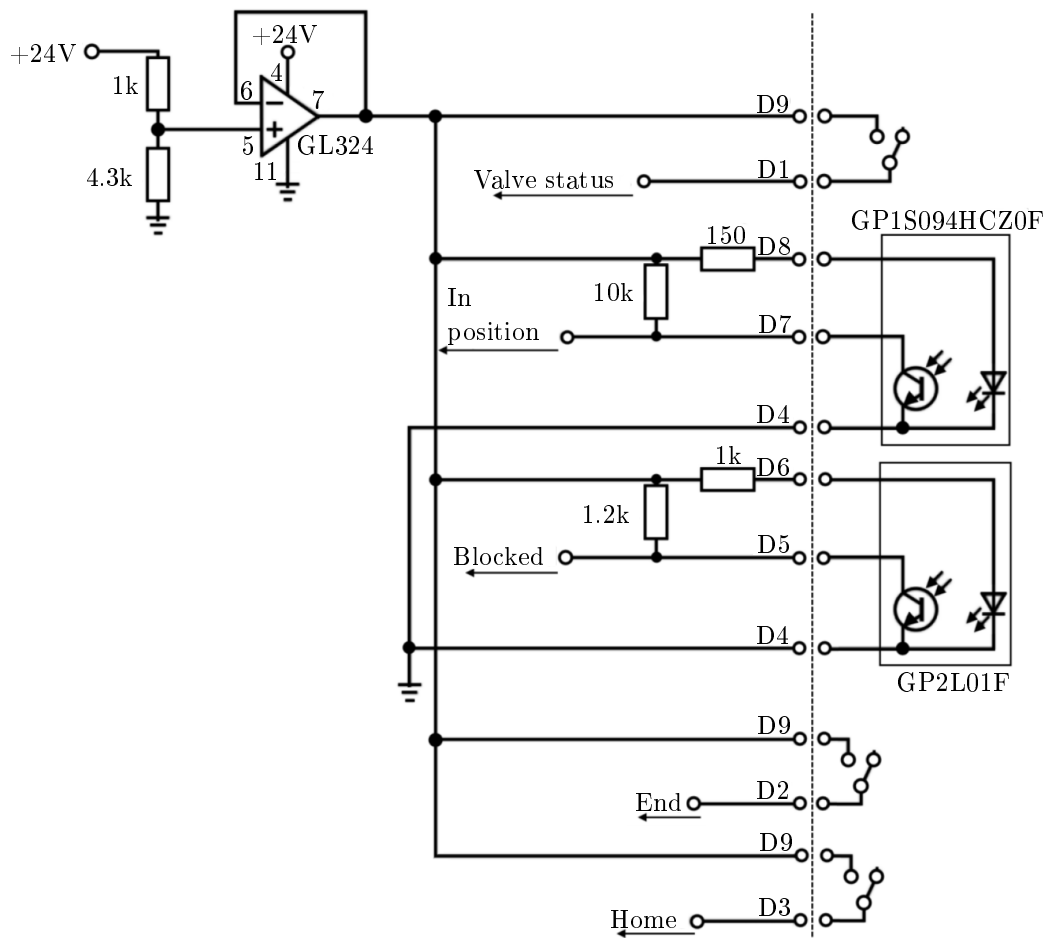


Figure 4.14: Sensor circuit diagram. The PCB board is on the left of the dashed line.

and detect it at the same time. If the LED light on the detector is detected, the sensor state is high, when the detector blocked, preventing light detection, the sensor state is low. When the photo interrupters are open, the 4.52 V value is read by the DAC giving a high state. This is thanks to the higher valued resistors, 10 k Ω and 1.2 k Ω . When the photo interrupters are open, the current begins to flow and voltage is reduced thanks to the resistors, lowering the voltage to value below the DAC detection threshold. The signal state is thus low and we know that the LED light is detected. First sensor in this group is GP1S094HCZ0F photo interrupter [27] giving the **In position signal**. As was mentioned in subsection 4.1.3, precise positioning of magazine is realised by position rods. When a position rod passes the photo interrupter, the LED signal is blocked giving high value of **In position** signal, stopping the magazine in this position. The second switch is GP2L01F reflective photo-interrupter [28] governing the **Blocked** signal. When a shuttle is holding a sample holder still partly inserted into a cassette slot, the LED light is reflected from the shuttle plate and a low value of **Blocked** signal is detected. This prevents heavy damage to the system by user error, when they try to move the magazine while holding a sample holder still placed inside it.

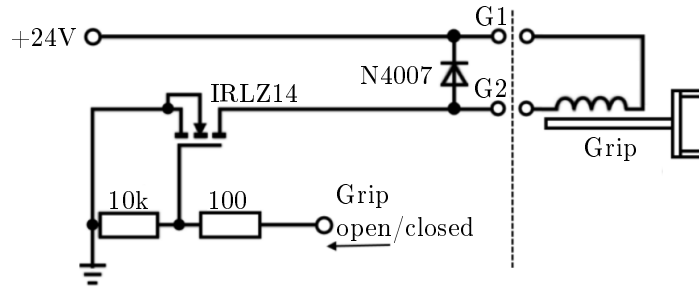


Figure 4.15: Grip control circuit diagram. The PCB board is on the left of the dashed line.

4.3.6 Grip control

The grip circuit is powered by 24 V PSU as shown in Figure 4.15. When the **Grip on/off** input signal is high, the IRLZ14 MOSFET switches to open state and the grip actuator is powered, opening the grip. When the input signal is low, the transistor switches back to off state and the grip closes. Circuit is protected from solenoid actuator voltage spikes by a N4007 flyback diode.

4.3.7 Control unit housing

The entire control unit is housed inside a 19-inch rack as shown in Figure 4.16 to allow mounting onto a rack stand. Insides of the rack can be seen in Figure 4.17. Both the circuit board and the power supplies are mounted onto DIN rails connected to the rest of the rack. To easily turn the system on and off, a power switch is installed. The rack is used as a protective ground connected to the rack stand to reduce chances of electrocution. Control board inputs and outputs are connected to the custom made backplate on the back side of the rack, see attachment RACK-BP. The backplate allows for mounting of DIN 45322 connectors [29] for I/O cable connection with the irradiation system as shown in Figure 4.18 and mounting of the power switch to turn the control unit on and off. The DAC is also attached to the backplate using double-sided adhesive tape.

The system housing allows for quick disassembly and removal of the control unit by unplugging all connectors and the DAC USB connector. Thanks to the addition of the DAC the system can be connected to any computer equipped with LabView and with the T5 control software available, allowing for a fast PC replacement in case of PC malfunction.

4.4 T5 Control software

The control unit alone can't realise irradiation process without instructions, these instructions are provided by the T5 control software written in LabView. The task of the software is to realise sample transfer between the **Target** position in the irradiation chamber, where the samples are irradiated, and the magazine as shown in Figure 4.19. The software also controls the shutter to provide the desired ion fluence over the ir-



Figure 4.16: Front view of control unit housed in a 19-inch rack.

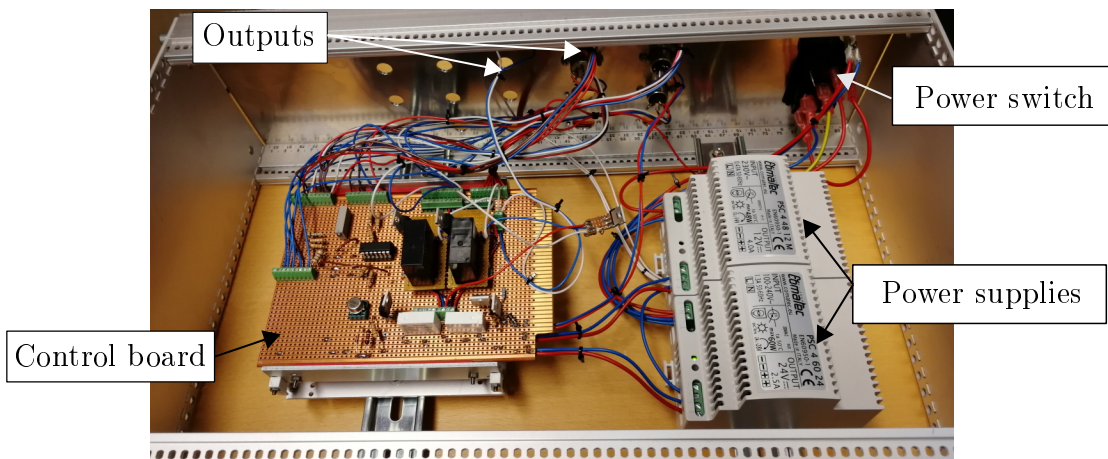


Figure 4.17: Insides of the control unit. Power supplies can be switched on and off by power switch. Control board outputs are on the back wall of the housing.

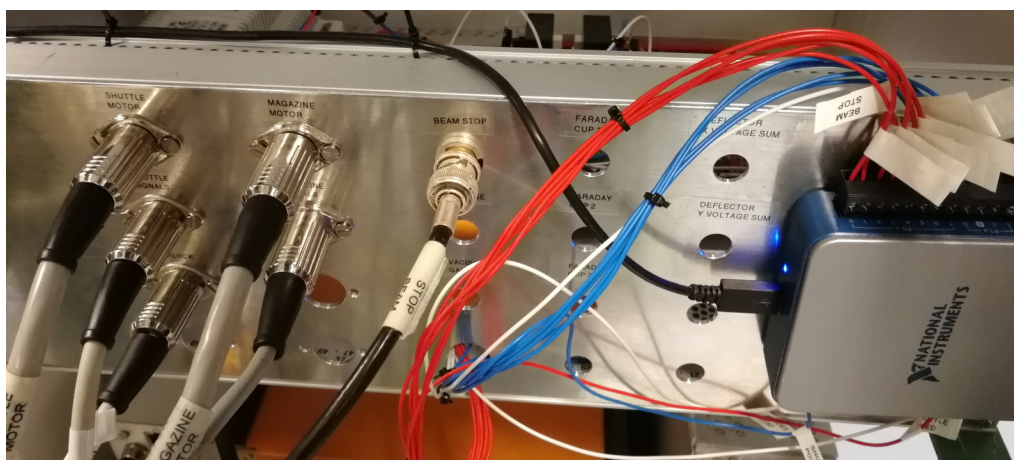


Figure 4.18: Back view of the control unit. National Instruments DAC card can be seen on the right side mounted onto the control unit. Output and input cables are labeled and connected to matching sockets.

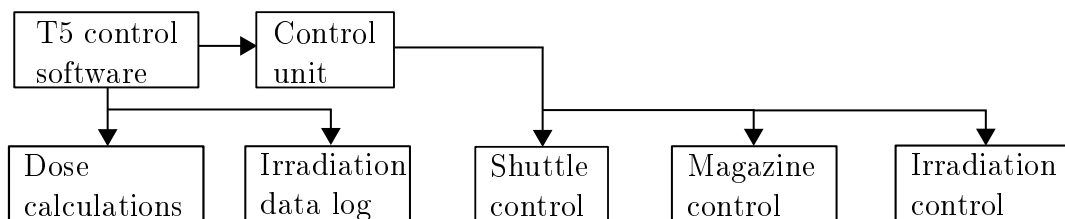


Figure 4.19: Schematic layout of the T5 control software.

radiated area and slightly automates the irradiation time calculation process. It also realises corrections to fluence for ion current fluctuation. Irradiation parameters during the experiment can be stored in the software and exported for further use. The software interface will be described in the following text, for further information on operation of irradiation beamline, see attachment T5 Manual.

4.4.1 Shuttle control

The shuttle control is realised using two panels in T5 control software, the shuttle control panel and position settings panel shown in Figure 4.20(a) and Figure 4.20(b) respectively. The shuttle control realises movement between magazine and irradiation chamber, the **Target** position, where sample is irradiated. To grab a sample from magazine, the shuttle must first move to the **Wait** position. When in the **Wait** position the sample holder can be grabbed by pressing the **Grab Sample** button, which opens the grip, approaches the sample holder, closes the grip, moves back and forth to click the grip pin in place and moves back to the **Wait** position. Being in **Wait** position is also required for returning the sample using the **Return Sample** button. At the start of the T5 control software, the shuttle movement is forbidden by default to prevent damage to the system in case of software error. To allow shuttle movement the **Shuttle ON/OFF** button has to be pressed.

The **Shuttle position** is continuously measured and shown in the shuttle control panel. When a **Target** or **Wait** button is pressed, the **Desired position** is set to corresponding value as shown in Figure 4.20(b). The shuttle movement direction is automatically set to reach desired position and motor is turned on. When the shuttle approaches the desired position, motor is turned off and shuttle decelerates until it stops at desired position.

Default **Target position** and **Wait position** values are shown in their respective windows in the position settings panel. Default values are loaded at the start of the software. To set new values, the values are entered in **Desired target position** and **Desired wait position** windows and set as new position values by pressing the **Set positions** button.

The shuttle control panel also contains three status indicators. The **In position/Moving** indicator tells us if the shuttle has reached its destination, or if it's still moving. The **Valve closed/open** shows if the gate valve between irradiation and magazine chambers is open or closed and the **Grip closed/open** status tells us if the grip is open or closed.

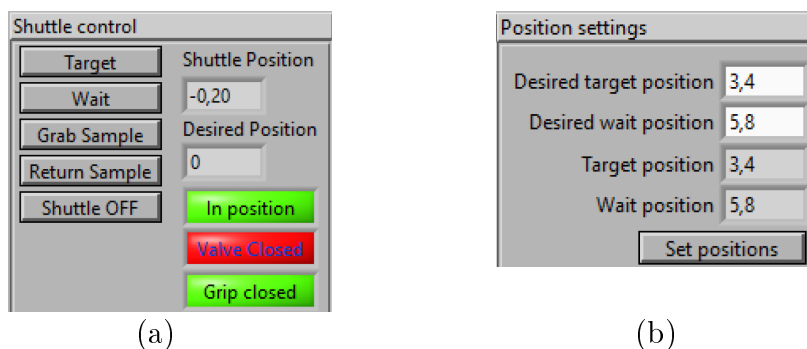


Figure 4.20: (a) Shuttle control panel and (b) position settings panel in T5 control software.

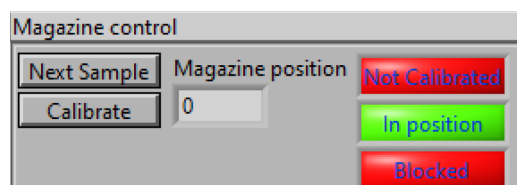


Figure 4.21: Magazine control panel in T5 control software.

4.4.2 Magazine control

The movement of the magazine is simpler than the movement of the shuttle as shown in Figure 4.21. First the magazine positions need to be calibrated by pressing **Calibrate** button. The **Calibrate** function moves the magazine towards the **Home** switch. When the switch is pressed, the movement direction is reversed and magazine's position rod triggers the **In position/Moving** photo-interrupter signal and the movement is stopped. Magazine's first slot is aligned with the shuttle now. To reach next slot position, the **Next Sample** button is pressed. Magazine moves forward until the **In position/Moving** photo-interrupter signal is triggered and the magazine stops. Current position can be seen in the **Magazine position** window.

The magazine control panel is also equipped with three indicators. The **Calibrated/Not Calibrated** indicator tells us if the system has been calibrated since the T5 control software launch, to remind the user to do so. The **In position/Moving** indicator shows if the the magazine is in position or still moving towards it and the **Blocked** status tells us if it is safe to move the magazine (green colour) or if it is dangerous to do so (red colour), because the shuttle is holding a sample holder inside the magazine.

4.4.3 Irradiation control

The precise control of the irradiation dose is achieved by irradiation control panel shown in Figure 4.22. The **Irradiation time** in seconds needed to reach desired can be entered into the window of the same name. When the time and beam is set and sample is in the **Target** position, the irradiation can be started by pressing the button labeled **Irradiate**. This will open the shutter and start to count the time from the

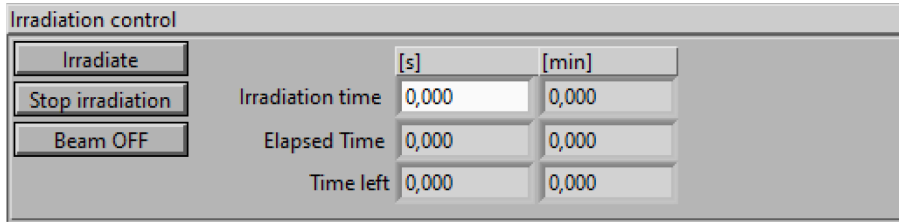


Figure 4.22: Irradiation control panel in T5 control software.

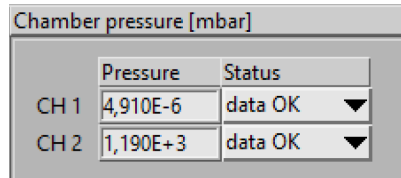


Figure 4.23: Chamber pressure panel in T5 control software.

start of the irradiation in the **Elapsed time** window and show the time left until the irradiation is finished in **Time left** window. When the **Elapsed time** value is equal to the **Irradiation time**, the shutter is closed. The irradiation can be stopped at any given time by the **Stop irradiation** button. If the irradiation is to be resumed after stopping, the **Time left** value in seconds needs to be inserted into **Irradiation time** window. The last function is the manual control of the shutter by pressing the **Beam ON/OFF** button, allowing us to turn the beam on or off at will. This function is used when the beam sweep and beam position are set before irradiations.

4.4.4 Chamber pressure

To monitor the irradiation comfortably from computer, the chamber pressure panel shown in the Figure 4.23 was added. This panel allows to monitor pressure in the main chamber, **CH1**, and magazine chamber, **CH2**. Pressure in both chambers is shown in milibars. Status of pressure gauges in both chambers is also shown, to warn us in case of malfunction or accidental disconnection.

4.4.5 Trouble shooting

Before we move onto the batch planner and automation control, we need to take a look at the trouble shooting panel shown in the Figure 4.24. In case the sample get's stuck and none of the basic control panels can solve the problem, the trouble shooting panels is used. It allows us to directly control shuttle direction and power to manually move the shuttle. Magazine direction can be also chosen and power turned on and off at will to stop in positions in between the positioning rods. Last but not least it allows for manual opening of grip to release stuck sample holders.

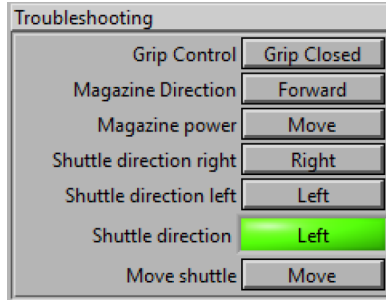


Figure 4.24: Trouble shooting panel in T5 control software.

4.4.6 Batch planner

The software was prepared with future automated irradiation sequence implementation in mind. This automation is realised by a batch planner window shown in Figure 4.25. The panel contains twenty lines to define parameters of samples mounted in the magazine. The first parameter that can be set is the **Status**, which tells us if the position is occupied by a sample or if it is empty. Then three informative data window follow allowing us to input the **Sample name**, beam **Ion species** and the ion beam **Energy**.

The next four values are used for irradiation time calculation. The **Irradiation time** can be calculated from ion's **Charge state**, the **Initial current**, the **Irradiated area** and the **Desired fluence** as

$$\text{Irradiation time} = \frac{\text{Charge state} \cdot \text{Irradiated area} \cdot \text{Desired fluence}}{\text{Initial current}}. \quad (4.1)$$

By pressing the **Set** button, the **Irradiation time** from the same row as the pressed button will be sent to the **Irradiation time** value in irradiation control panel. This allows us to input and calculate irradiation times with ease. The **Total time** shown on the lower right of Figure 4.25 is a sum of all irradiation times in the table. This corner also contains the button to irradiate all non empty slots in the table, this function is to be implemented in the future. At the moment the **Run** button does nothing.

The **Irradiated area** can also be calculated from current measurements using two Faraday cups. First Faraday cup is located before the switching magnet and measures total beam current. Second Faraday cups is in the middle of the Faraday cup array in irradiation chamber. Area of this Faraday cup is 1 cm^2 , allowing for direct measurement of swept beam current density. If we say that the area is homogeneously irradiated, we can calculate this area as

$$\text{Irradiated area} = \frac{FC_{\text{Switching magnet}}}{FC_{\text{Swept beam}}} \cdot 1 \text{ cm}^2, \quad (4.2)$$

allowing alternate method of area calculation instead of optical evaluation of the swept beam area. The calculated area can be set to all positions that are not empty by the **Set** button on lower left part of the Figure 4.25.

The dose received by the sample can be corrected by entering **Final current** at

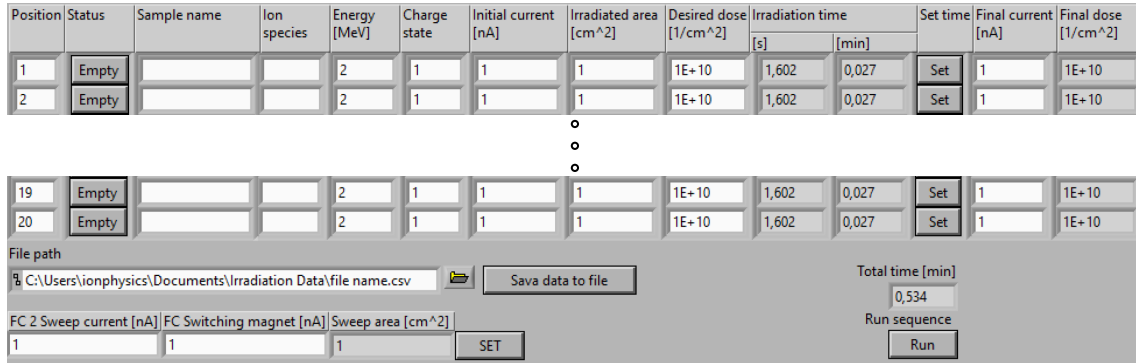


Figure 4.25: Batch planner panel in T5 control software.

the end of irradiation. **Final dose** received by the sample is then calculated as

$$\text{Final dose} = \text{Initial fluence estimate} \cdot \frac{\text{Initial current} \cdot \text{Final current}}{2 \cdot \text{Initial current}}. \quad (4.3)$$

As the ion source and accelerator stabilize at the beginning of a session, or as a sputter target is consumed over the course of a long run, the beam current can both increase and decrease. As such, Equation 4.3 is a first order improvement of the initial fluence estimation.

The entire batch planner window can be saved to a .csv file for further edition. To save it, the **File path** must be entered into the window alongside a file name. The file is then saved by pressing the **Save data to file button**.

4.4.7 Future modifications

The basic functionality of the system with new computer has been achieved and sample transfer reliability improved, but there is still room for further improvement. The first and most important step in the future is implementation of automated irradiation of entire magazines. Importance of this improvement is both in the user time saved during irradiation experiments and in the safety of operation. If ion beams that produce gamma radiation are used during irradiation runs, the user presence near the chamber has to be kept at minimum to lower the radiation dose and prevent health issues.

The next thing to make lives of users easier would be Faraday cup current reading inside the T5 control software, right now an external laptop connected to the tandem accelerator control software has to be used to read current values while operating the irradiation beamline. Without the laptop a lot of running back and forth between the beamline and control center has to be made. The automated irradiation would greatly benefit from this addition as well. If current could be measured after each sample, we would be able to monitor the current changes through time and improve the final fluence calculation by a fit of the measured current values vs. time.

The last improvement that comes to mind is a connection of the camera used to adjust the beam sweep area to beamline PC. It would allow us to watch and control the irradiation process remotely without the need to watch external screen in person at the beamline as shown in Figure 4.26. Users would be able to set a mask around

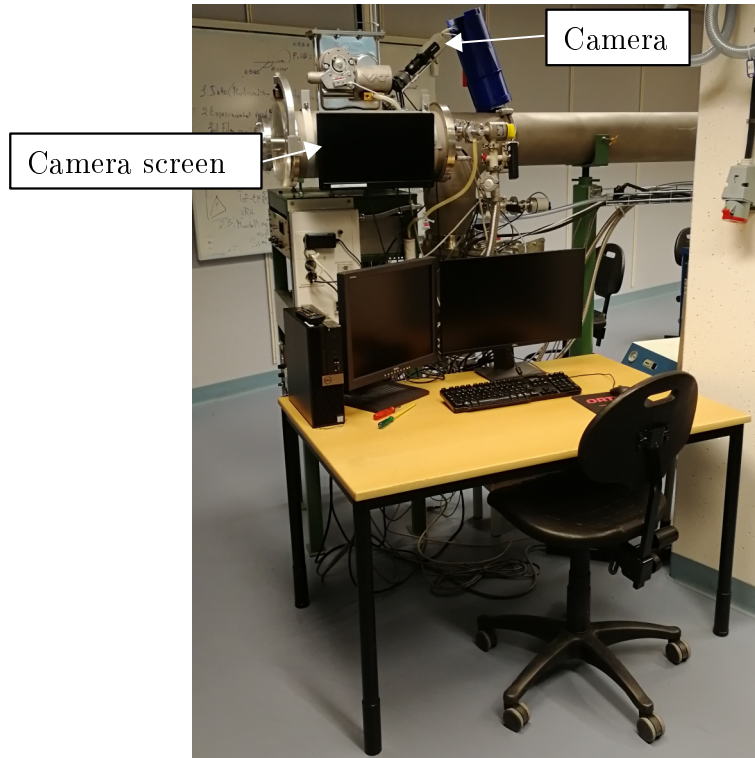


Figure 4.26: Irradiation beamline operator workplace. Camera and connected screen are shown.

the irradiated area to see if all samples mounted on sample holder are irradiated.

5. Germanium quantum dot irradiation

To show an experimental application of the irradiation beamline, the germanium quantum dot, Ge QD, irradiation experiment was chosen. The Ge QDs were manufactured at the Johannes Kepler University Linz using molecular beam epitaxy on a pit patterned silicon substrates as described in [30, 31, 32] and shown in Figure 5.1. Optical properties of these Ge QDs were studied, see [30, 33, 31] for details, and applications in integrated optics are researched [34, 35]. Various methods to improve the light emission of the structure have been used [36, 37, 38]. The field of light emission improvement is where the ion irradiation was used. The goal was to improve photoluminescence, PL, of Ge QDs by ion induced defects in the material [39]. The following text will deal with the experiment, starting from a sample preparation, going through the irradiation process and ending with PL measurement results.

5.1 Sample irradiation

Before the irradiation takes place, the irradiation parameters have to be decided. First the ion species are chosen alongside desired energies. Then the ion fluence is picked. But before we delve into the experimental details, we will begin with another important part of the experiment, the sample preparation.

5.1.1 Sample preparation

The Ge QDs fabricated on Si wafers were manufactured using two voltages during the molecular beam epitaxy, each of the two irradiated wafers had different value. The first

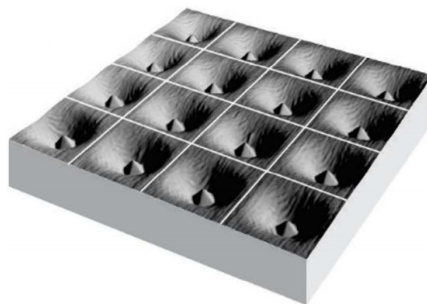


Figure 5.1: Ge QD shape illustration. (Edited from [31])

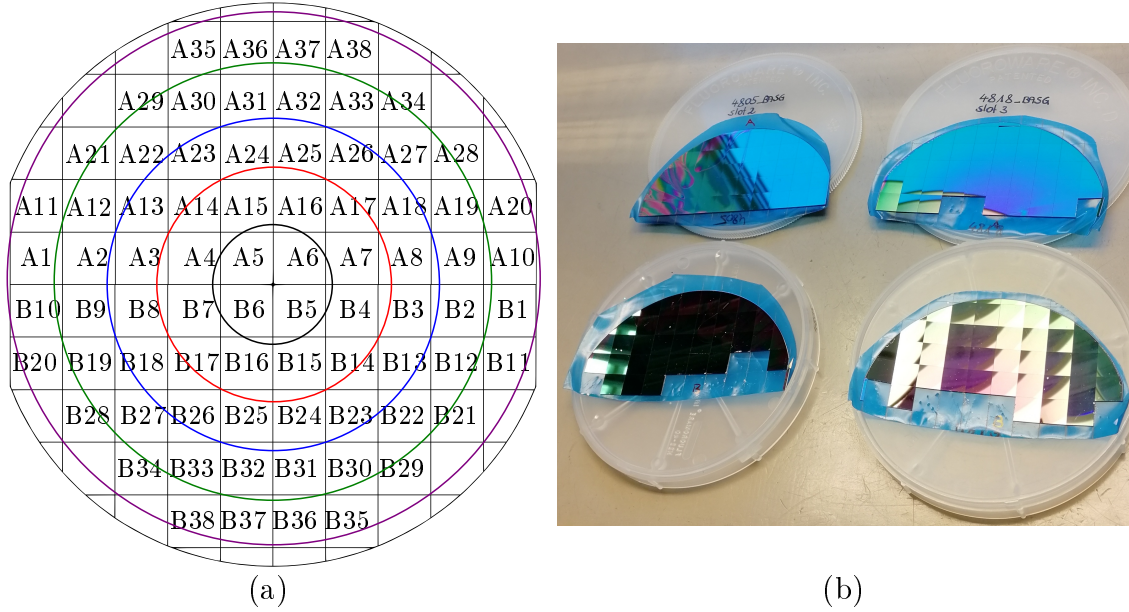


Figure 5.2: Ge QD samples. (a) Sample labeling. Letter denotes half of the wafer and number the position on said half. Circles denote distances from center of the wafer used as references during the photoluminescence measurement. (b) Photo of sample wafers.

wafer labeled as 4805 was deposited with the wafer grounded, while the second labeled 4818 was deposited at a floating wafer voltage. The wafers were cut into squares of approximately $10 \times 10 \text{ mm}^2$ and separated into halves as shown in Figure 5.2(b). The samples were labeled by the wafer label to know from which wafer the sample is, a letter denoting which half of the wafer they came from and number to designate the sample's position on said half as shown in Figure 5.2(a). The samples were then bathed in acetone and isopropyl alcohol ultrasonic baths for 7 minutes each to strip the protective resist layer before mounting on sample holders.

5.1.2 Irradiation parameters

The sample holders were then loaded into the magazine and irradiated using carbon and chlorine ions at various energies and fluences as shown in attachment Irradiation parameters. The ion species were picked to have a dominant electric stopping over the nuclear stopping in order to make the QDs amorphous and induce recrystallisation in the material. Two energies were picked for each ion species to provide more variety in stopping parameters. Three ion fluence values were chosen to allow study of PL dependence on ion fluence. Samples were irradiated at pressure of $5 \cdot 10^{-6}$ mbar to limit contamination from the remaining atmosphere.

5.2 Photoluminescence measurements

After the irradiation was finished the samples' PL was measured at Johannes Kepler University Linz. But before we get to the experimental results, we will provide the

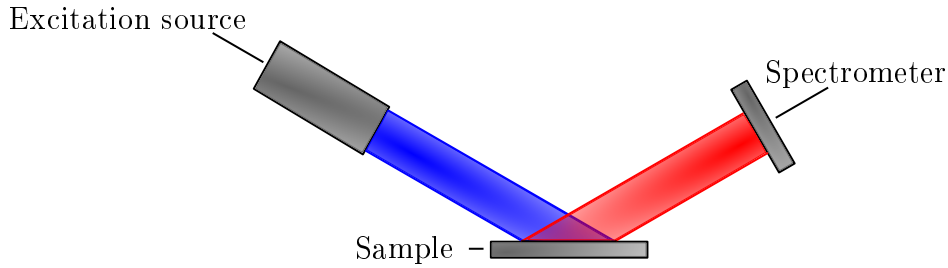


Figure 5.3: PL principle schematic. Radiation from excitation source excites the electronic states of the sample. Radiation intensity from deexcitations is then measured by spectrometer with dependence on radiation wavelength, giving us PL spectra as an output.

theoretical basis of photoluminescence measurements.

A schematic of PL principle can be seen in Figure 5.3. The sample is irradiated by a light source of wavelength from UV or near UV part of the light spectrum. The incoming light excites the electronic states in the sample and the excitation can be released by both radiative and non radiative processes. If the deexcitation is radiative, we call it photoluminescence. The photoluminescence can be further categorised by the nature of the electronic transitions, see [39] for more details.

5.2.1 Results

PL of samples were measured at room temperature. From previous QD experiments it was known that the PL intensity falls from the center of the wafer towards it's edges by a factor of three. A reference measurements on irradiated samples were made at a defined distance steps from the center of the wafer towards it's edges as seen in Figure 5.2(a). A reference nonirradiated samples were taken from each of these rings to measure default PL before irradiation process for comparison with specimens modified by the ion fluence. Spectra of these reference samples from wafer 4805 can be seen in Figure 5.4. The PL intensity was measured at a wavelength range from 1100 nm to 1600 nm where the Ge PL peak is present. A small Si peak can be seen on the left side of the spectrum. The PL intensity falloff on samples away from the center can be clearly seen.

The next step was measurement of the irradiated samples. Samples were measure at a wavelength range from 1100 nm to 1600 nm and the relative PL intensity was then calculated by using integrated intensity values of irradiate samples and reference samples using formula

$$\text{Relative PL intensity} = \frac{\text{Sample PL intensity}}{\text{Reference PL intensity}} \quad (5.1)$$

The intensity of reference samples at zero fluence was set as value 1. The relative PL intensities were then plotted over ion fluence used during irradiation, which can be seen in Figure 5.5. We didn't achieve the goal of increasing PL intensity by inducing defects in the material, we achieved the exact opposite, PL intensity decrease with ion

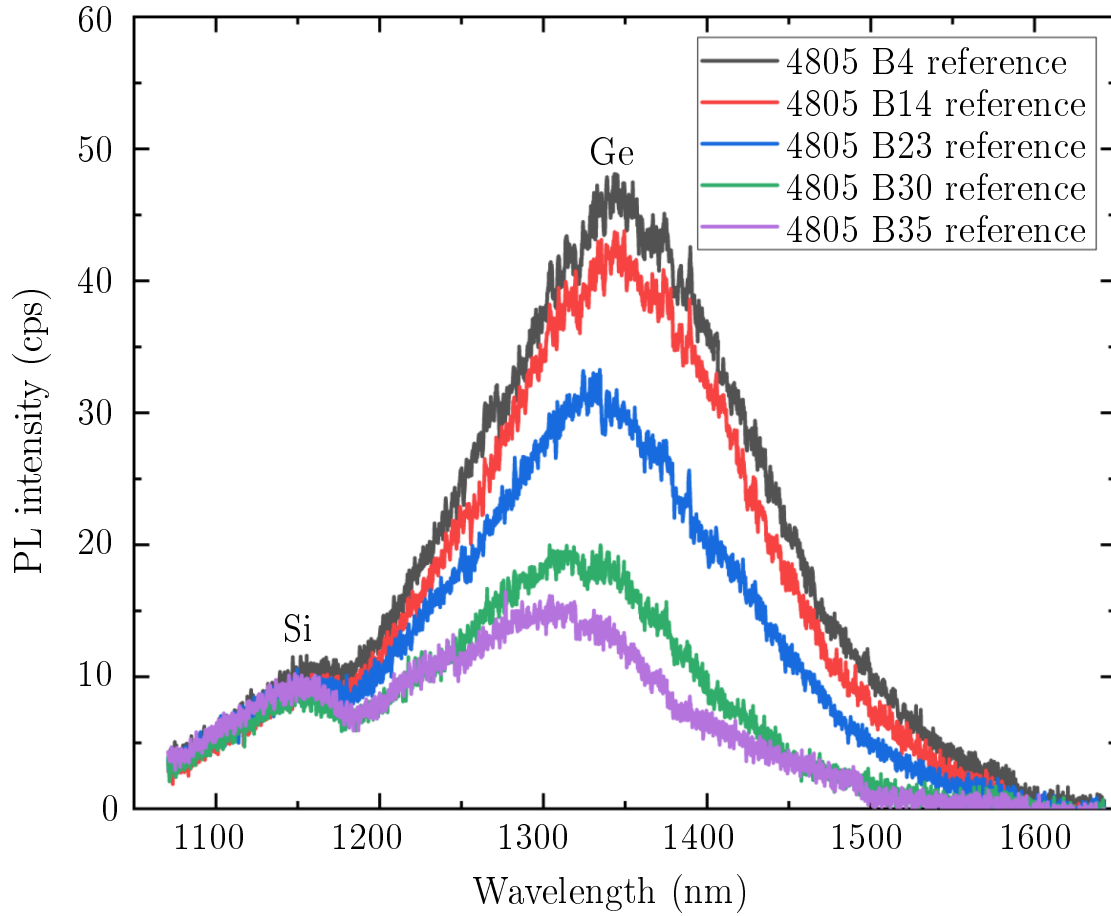


Figure 5.4: Reference PL measurements. The Ge peak PL intensity decreases from the center of the wafer towards the edges, where the intensity is lower by a factor of 3. A small Si substrate peak is visible on the left side of the intensity spectrum.

fluence. For the future MeV ion irradiations of Ge QDs a more careful assessment of the electronic and nuclear stopping powers as well as projectile range in the target have to be made in order to achieve desired outcome.

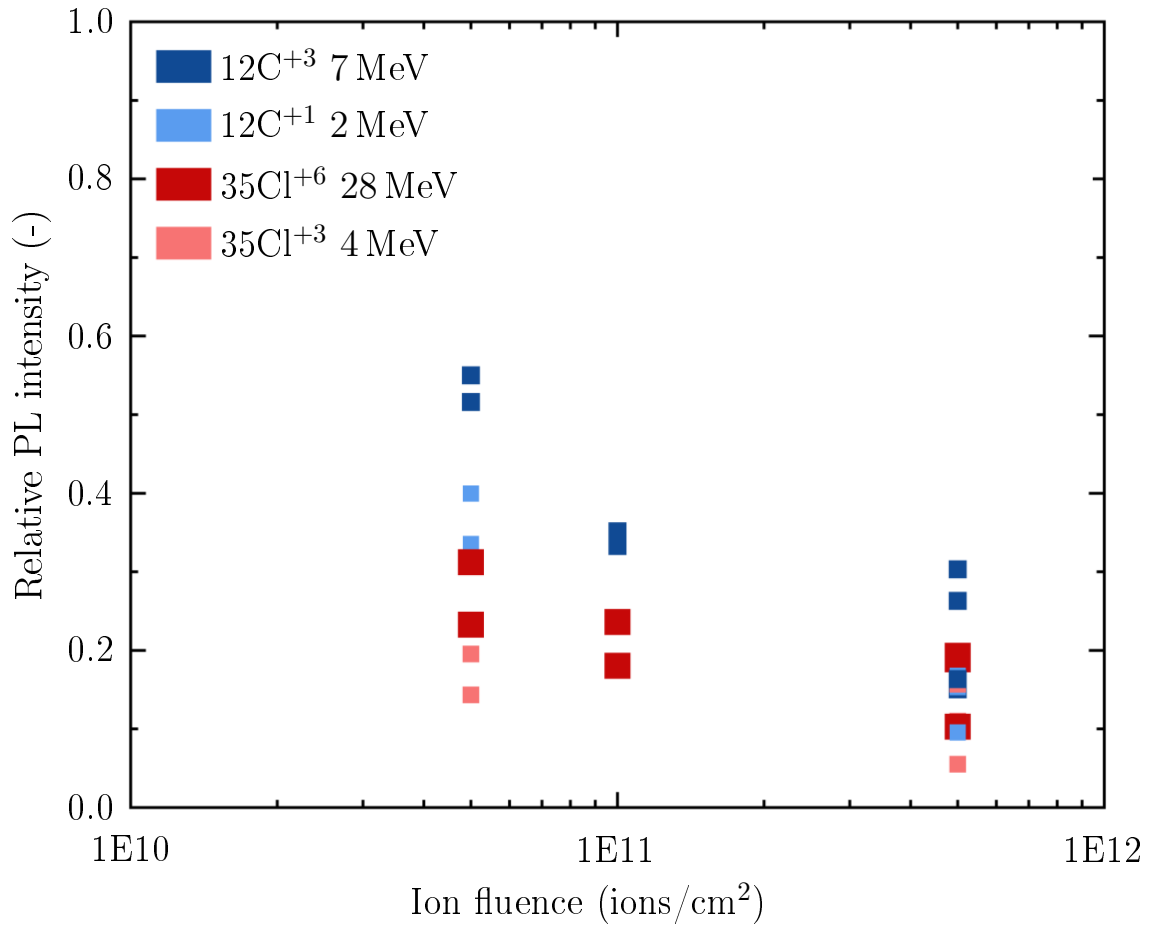


Figure 5.5: Irradiated samples PL intensity relative to non irradiated samples and their dependence on ion fluence. We can see that the relative PL intensity decreases with increasing fluence. Different ion species cause diverse PL intensity decrease. This decrease is bigger for lower projectile energies.

6. Irradiation homogeneity

A main parameter of irradiation experiments is the ion fluence, the amount of ions impinging on solid's surface per unit area. In order to reproduce same experimental conditions, knowing only ion fluence is a bit problematic. If the ion fluence is not uniform over the entire irradiated area, it is hard to repeat the same experiments. In order to test the uniformity of ion fluence or irradiation homogeneity a simulation was made in a MATLAB software [3] to see the influence of electrostatic deflector sweeping frequencies on ion fluence homogeneity. Homogeneity will be sufficient if no patterns arising from sweeping frequencies are present. This simulation will be described in the following text beginning with a theoretical model and ending with simulation results. See attachment Homogeneity simulation for entire code with comments.

6.1 Theoretical model

In order to simulate a ion distribution on the sample a beam needs to be defined. In our case the beam was defined as a Gaussian distribution of particles on a circle of diameter D as shown in Figure 6.1. Gaussian function

$$f(x) = \frac{1}{\sigma\sqrt{2\pi}} e^{-\frac{1}{2}\left\{\frac{x-\mu}{\sigma}\right\}^2} \quad (6.1)$$

was used, where x is a free variable defining the position, μ is the mean value of the distribution and σ is the standard deviation [40]. The standard deviation σ was chosen to make 95 % of particles to be generated within the defined interval, in our case the diameter D. To make this possible the σ must fulfill the equation

$$2\sigma = \frac{D}{2}, \quad (6.2)$$

giving the standard deviation

$$\sigma = \frac{D}{4}. \quad (6.3)$$

This Gaussian distribution was used in 2D, in x and y directions, to generate a beam spot as shown in Figure 6.2, where 10^6 particles were created with positions in x and y given by Gaussian distribution in each direction. Particles were then binned by their positions in 1000×1000 bins, 1000 bins for each direction, and particles per bin are shown.

In the next step, the particles are assigned kinetic energy E_k in MeV and the velocity

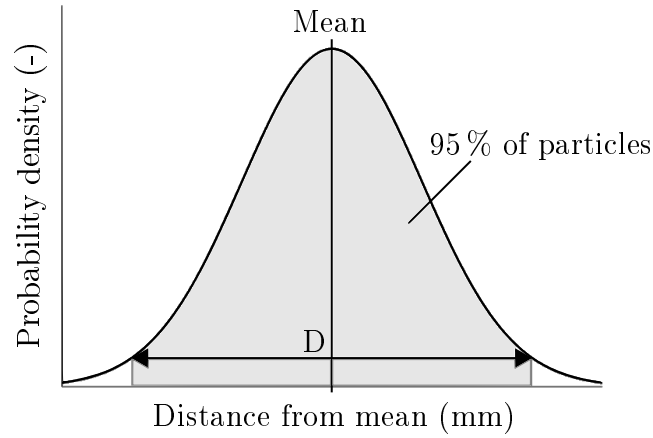


Figure 6.1: Gaussian beam irradiation distribution of the spot in x and y directions. The distribution was defined with standard deviation $\sigma = D/4$ to achieve that 95% of particles are located within circular spot of diameter D centered around the mean value.

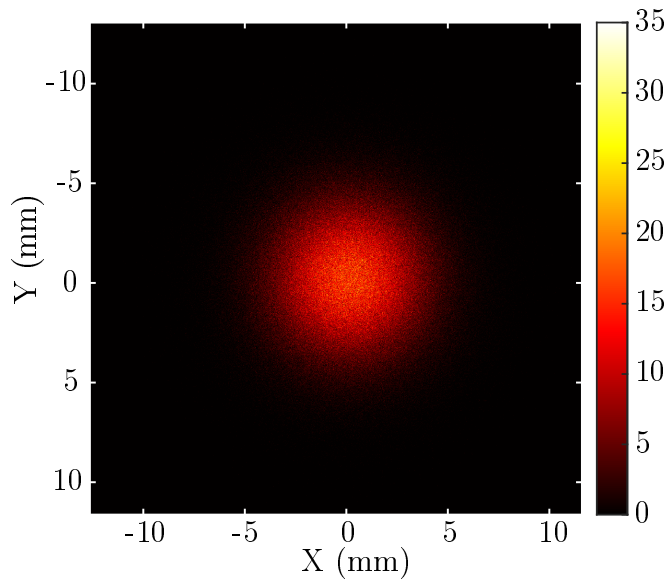


Figure 6.2: Gaussian beam spot made of $N = 10^6$ particles with X and Y coordinates generated by a Gaussian distribution with $\sigma = 2.5$ mm on a circle with diameter $D = 10$ mm. The resulting particle array was then binned with 1000 bins for both X and Y direction. Color indicates the number of particles in a corresponding bin.

of particles, v_z , alongside the system axis shown in Figure 6.3, the z direction, is given as

$$v_z = \sqrt{\frac{2E_k}{m}}, \quad (6.4)$$

where m is the mass of the particle [41]. The relativistic correction was neglected. Using v_z the times, T_x and T_y , it takes the particle to travel between deflector plates of length L_x and L_y and times, t_x and t_y , it takes it to travel the distance l_x and l_y from the deflector plates to the target can be calculated as

$$T_x = \frac{L_x}{v_z} \quad T_y = \frac{L_y}{v_z} \quad t_x = \frac{l_x}{v_z} \quad t_y = \frac{l_y}{v_z}. \quad (6.5)$$

The acceleration between the plates can then be calculated from the electric force

$$F = ma = Eq, \quad (6.6)$$

where q is the charge state of the particle and E is the electric field strength between the plates given by

$$E = \frac{V}{d}, \quad (6.7)$$

where V is voltage between the plates and d their separation. The voltages V_x and V_y are defined by a triangular waves of frequencies 64 Hz and 517 Hz for x and y deflector respectively. The particles are entering the deflectors with time steps

$$\delta t = \frac{t_1}{N}, \quad (6.8)$$

where t_1 is a irradiation time defining how long the irradiation is and N is the total amount of particles. The first particle is entering at time $t_1 = 0$, the second particle at time $t_2 = \delta t$, the third at $t_3 = 2 \cdot \delta t$ and so on. The voltage changes during an ion's transfer time through the unit are neglected.

Accelerations in x and y directions can then be expressed as

$$a_x = \frac{V_x q}{md} \quad a_y = \frac{V_y q}{md}. \quad (6.9)$$

Velocities of particles leaving the deflector plates are

$$v_x = a_x T_x \quad v_y = a_y T_y \quad (6.10)$$

and positions of particles when impinging upon the sample can be calculated as

$$X = X_0 + \frac{1}{2} a_x T_x^2 + v_x t_x \quad Y = Y_0 + \frac{1}{2} a_y T_y^2 + v_y t_y, \quad (6.11)$$

where X_0 and Y_0 are the initial coordinates of the particle before sweeping, the second term is a linearly accelerated motion between the deflector plates and the last term describes free movement between the deflectors and the sample, see Figure 6.3.

Using this simulation we can transform beam spot defined by an array to swept

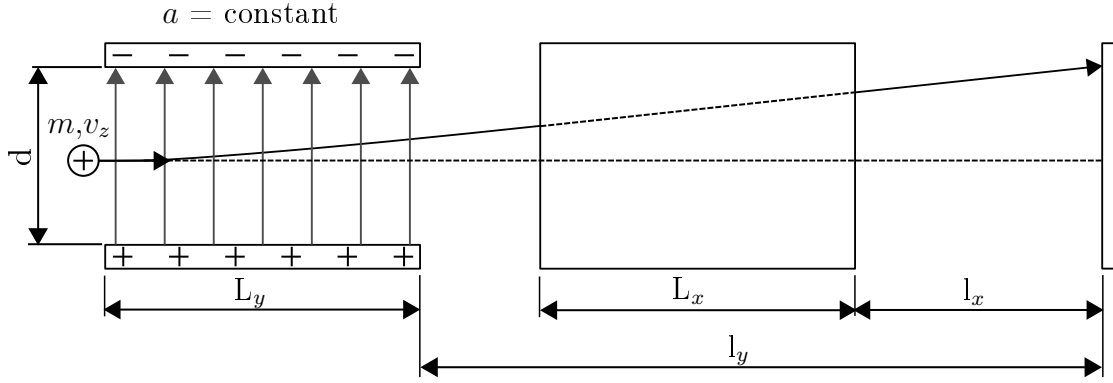


Figure 6.3: Deflector simulation schematic. Acceleration between deflector plates of lengths L_x , L_y and separation d is approximated by a constant value and ions are thus uniformly accelerated between the deflector plates gaining velocities v_x and v_y . Ions move at constant velocity at distances l_x and l_y between the deflector and the sample.

Table 6.1: Constant parameters used during calculations. L_x , L_y - deflector plate lengths, l_x , l_y - deflector to target distance, d - plate separation, E - beam energy, V_x , V_y - deflector voltages, f_x , f_y - deflector sweep frequencies, D - beam diameter.

L_x (m)	L_y (m)	l_x (m)	l_y (m)	d (m)	E (MeV)	V_x (kV)	V_y (kV)	f_x (Hz)	f_y (Hz)	D (mm)
0.50	0.57	4.5	5.27	0.06	5	10	10	64	517	10

beam array on the sample's surface. The swept beam array is defined by the deflector plate voltage amplitudes, the irradiation time t_I , the number of particles N and the particle parameters, the mass m and the kinetic energy E . The swept beam array is then binned in the same manner as the beam spot array to give images in the following text.

6.2 Results

The simulation was ran for protons, $m = 1 \text{ Da}$ and $q = 1 \text{ C}$, with constant parameters shown in Table 6.1. The irradiation time t_I , the number of particles N and binning were changed to test the uniformity of ion fluence.

The first uniformity test was realised with a constant number of impinging ions $N = 10^6$ and varying irradiation time t_I , giving a varying flux of ions. Four time values were chosen with 1000×1000 binning as shown in Figure 6.4. Bin area is approximately $(120 \times 100) \mu\text{m}^2$. No patterns arising from sweeping frequencies are present and ion fluence can thus be declared as uniform for different ion fluxes.

The second test was a spatial uniformity check, where $N = 10^6$ and $t_I = 125 \text{ s}$ were chosen and binning values were changed as shown in Figure 6.5. We started at binning of 100×100 and went up to 1000×1000 as in the first test. There are also no sweep patterns or inhomogeneities present. Spatial uniformity can thus be declared uniform.

The last test was irradiation homogeneity evolution through time. A defined amount

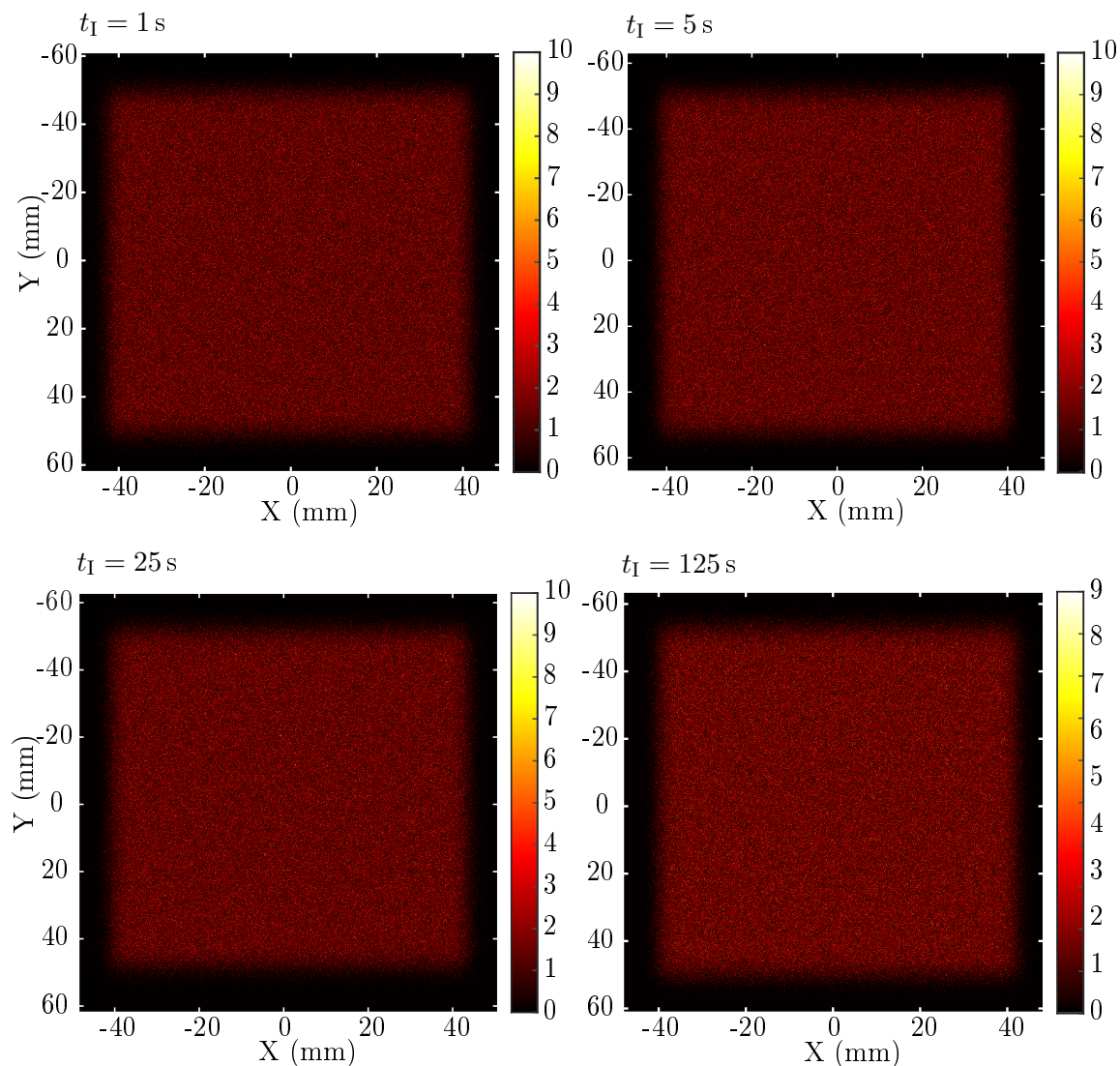


Figure 6.4: Irradiation homogeneity with a varying irradiation time t_I . $N = 10^6$, binning 1000×1000 . Color indicates the number of particles in a corresponding bin. No patterns arising from sweep frequencies are present. Irradiation is uniform in time for constant ion fluence and varying ion flux.

of $N_t = 10^4$ ions impinged upon the sample surface per second. The irradiation homogeneity is observed at four time stamps as shown in Figure 6.6. We see no sweep patterns in the ion distribution on sample's surface and thus we declare the sample surface ion fluence uniform in time.

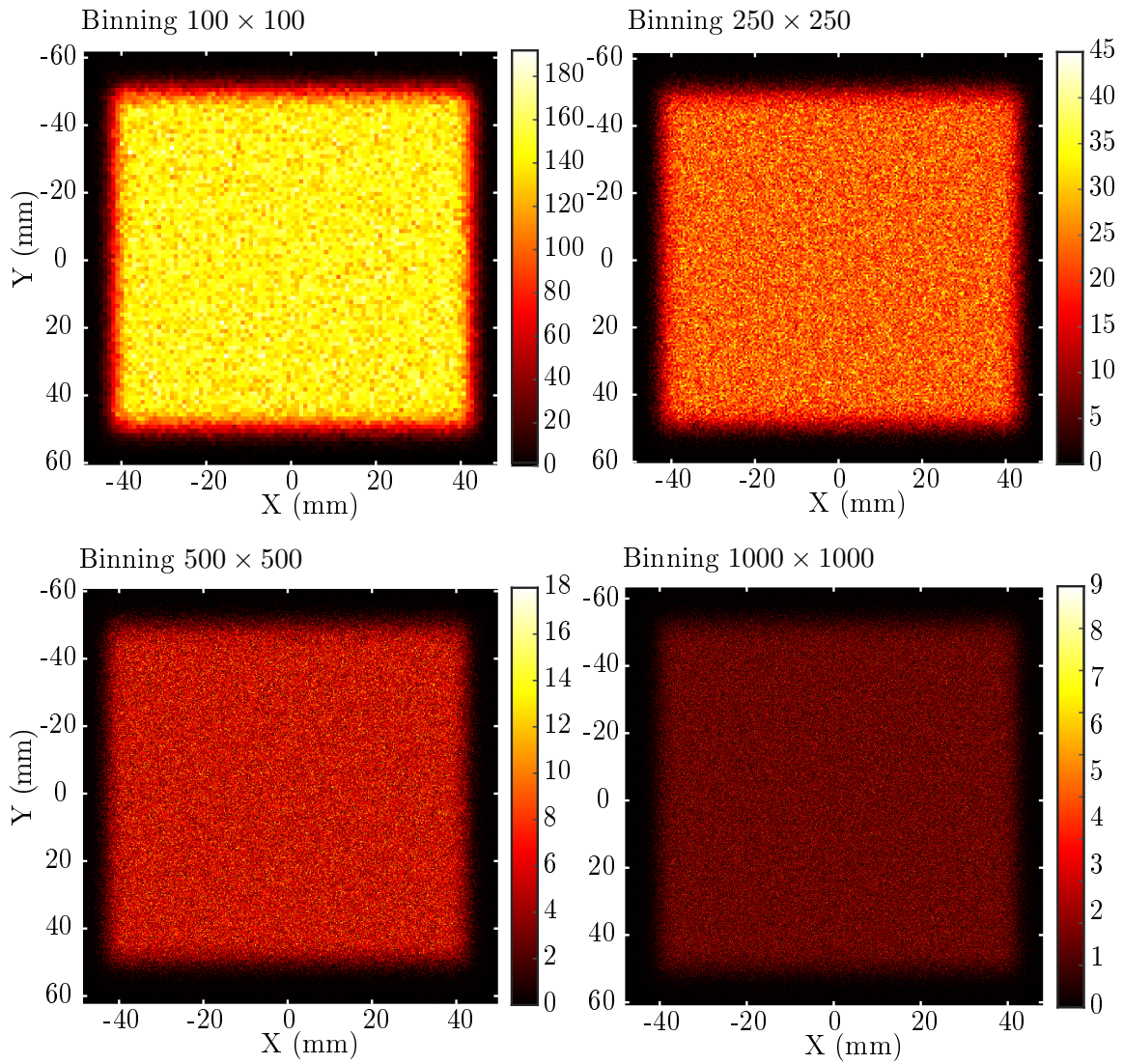


Figure 6.5: Irradiation homogeneity with with varying binning values and $N = 10^6$. Color indicates the number of particles in a corresponding bin. No sweeping patterns are present and irradiation is declared spatially homogeneous.

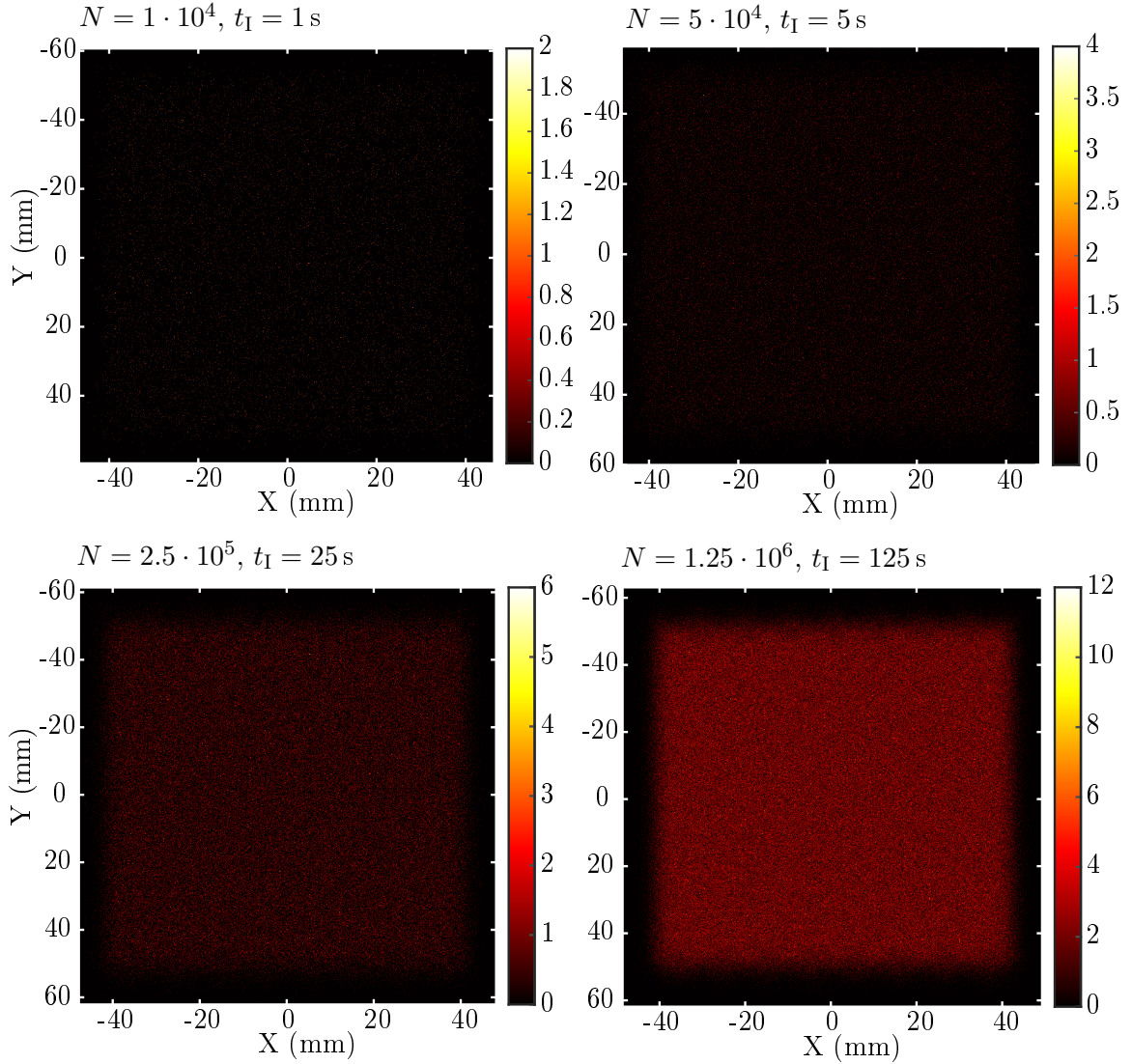


Figure 6.6: Time evolution of irradiation homogeneity. $N_t = 10^4$ ions impinge upon the surface per second. Total ions impinging upon sample N alongside irradiation time t_I are shown at defined time steps with binning 1000×1000 . Color indicates the number of particles in a corresponding bin. We can see that no patterns appear during the irradiation process.

7. Conclusions

We have introduced the irradiation beamline at Uppsala University's Tandem Laboratory in its previous state and its applications in material science. The theory of ion irradiation was briefly reviewed and the working principle of the entire instrumentation was presented starting from the ion sources, going through the Tandem accelerator and ending on the irradiated sample.

Then we moved onto the main topic of this thesis, the improvements and modifications implemented to the irradiation beamline setup. We began this topic with the improvement to the shuttle's grip mechanism that increased the sample transport reliability by decreasing chances of accidental sample dropping in the vacuum and minimising transfer system misalignments. Next we presented the control unit replacement that allowed us to use modern computers with more recent operating systems. The new control unit is connected to a PC using an USB connector allowing for compatibility with any computer, that has LabView installed and has T5 control software application on it, allowing for an easy replacement in case that the connected PC malfunction.

The T5 control software realises automation and simplification of most functions. That makes the beamline controls easy to learn and use for experiments. Future steps to improve the user experience would be implementation of a batch mode allowing to run up to 20 samples autonomously by defining irradiation parameters in advance and addition of more precise dose correction calculation method instead of the linear interpolation, to achieve more precise dose values with minimal error. This could be achieved by implementing a current measurement functionality into the control unit or by usage of an external ampere meter.

The capability of the modified and improved irradiation beamline was demonstrated on the Ge QD irradiation experiment that ended in failure from the PL improvement point of view, but shown that the system control unit works as intended and can be used without worries in future experiments. This was further proved by irradiation homogeneity calculations that have shown the uniformity of ion fluence on the sample with varying ion flux, and thus current. Irradiation homogeneity was also shown to hold through prolonged periods of time. The simulation results should be compared to experimental data in the future.

In the end we can say that the irradiation beamline setup has been successfully improved to keep up with advances in technology. The system was made simple to use and the users can quickly start to irradiate their samples for their research and applications. The ease of use and simpler control of irradiation parameters could increase the usage of the beamline in the future and allow the wide area of applications

of MeV ion irradiation to be further expanded and maybe allow the setup to work in new and interesting research areas.

References

1. HALLÉN, A.; INGEMARSSON, P.; HÅKANSSON, P.; SUNDQVIST, B., et al. An MeV-ion implanter for large area applications. *Nuclear Instruments and Methods in Physics Research Section B: Beam Interactions with Materials and Atoms*. 1989, **36**(3), 345–349. ISSN 0168-583X. Available from DOI: 10.1016/0168-583X(89)90679-4.
2. *LabView* [online]. National Instruments Corporation, 2021 [visited on 2021-04-02]. Available from: <<https://www.ni.com/cs-cz/shop/software/products/labview.html>>.
3. *MATLAB* [online]. The MathWorks, Inc., 2021 [visited on 2021-04-20]. Available from: <<https://www.mathworks.com/products/matlab.html>>.
4. NASTASI, M.; MAYER, J.; HIRVONEN, J. K. *Ion-Solid Interactions: Fundamentals and Applications*. Cambridge: Cambridge University Press, 1996. ISBN 9780521373760.
5. *Electronic Stopping Power of Matter for Ions* [online]. Vienna: Vienna International Centre, 2007-2021 [visited on 2021-02-14]. Available from: <<https://www.iaea.org/resources/databases/stopping-power>>.
6. ZIEGLER, J. F.; ZIEGLER, M.; BIRSACK, J. SRIM – The stopping and range of ions in matter (2010). *Nuclear Instruments and Methods in Physics Research Section B: Beam Interactions with Materials and Atoms*. 2010, **268**(11), 1818–1823. ISSN 0168-583X. Available from DOI: 10.1016/j.nimb.2010.02.091.
7. BIRSACK, J.; HAGGMARK, L. A Monte Carlo computer program for the transport of energetic ions in amorphous targets. *Nuclear Instruments and Methods*. 1980, **174**(1), 257–269. ISSN 0029-554X. Available from DOI: 10.1016/0029-554X(80)90440-1.
8. DINIA, A.; AYOUB, J.; SCHMERBER, G.; BEAUREPAIRE, E., et al. Effect of ion irradiation on the structural and the magnetic properties of Zn_{0.75}Co_{0.25}O magnetic semiconductors. *Physics Letters A*. 2004, **333**(1), 152–156. ISSN 0375-9601. Available from DOI: 10.1016/j.physleta.2004.10.027.
9. FASSBENDER, J.; MCCORD, J. Magnetic patterning by means of ion irradiation and implantation. *Journal of Magnetism and Magnetic Materials*. 2008, **320**(3), 579–596. ISSN 0304-8853. Available from DOI: 10.1016/j.jmmm.2007.07.032.

10. SOM, S.; DUTTA, S.; KUMAR, V.; KUMAR, V., et al. Swift heavy ion irradiation induced modification in structural, optical and luminescence properties of Y₂O₃:Tb³⁺ nanophosphor: Tb³⁺ nanophosphor. *Journal of Luminescence*. 2014, **146**, 162–173. ISSN 0022-2313. Available from DOI: 10.1016/j.jlumin.2013.09.058.
11. ZHANG, H.; ZHANG, C.; YANG, Y.; MENG, Y., et al. Irradiation hardening of ODS ferritic steels under helium implantation and heavy-ion irradiation. *Journal of Nuclear Materials*. 2014, **455**(1), 349–353. ISSN 0022-3115. Available from DOI: 10.1016/j.jnucmat.2014.06.062.
12. WAS, G.; JIAO, Z.; GETTO, E.; SUN, K., et al. Emulation of reactor irradiation damage using ion beams. *Scripta Materialia*. 2014, **88**, 33–36. ISSN 1359-6462. Available from DOI: 10.1016/j.scriptamat.2014.06.003.
13. HINTERBERGER, F. Electrostatic accelerators. *CAS 2005 - CERN Accelerator School: Small Accelerators, Proceedings*. 2006/01/01, 95–112. Available from DOI: 10.5170/CERN-2006-012.95.
14. ROGERS, E. J. Optimal selection of sweep frequencies in ion implantation systems with X-Y scanning. *Nuclear Instruments and Methods in Physics Research*. 1981, **189**(1), 305–310. ISSN 0167-5087. Available from DOI: 10.1016/0029-554X(81)90159-2.
15. *E03600341500S Tension Spring* [online]. Sodemann Industriefjedre A/S., 2020 [visited on 2021-04-02]. Available from: <<https://www.industrial-springs.com/e03600341500s>>.
16. *Kuhnke H6206-F 24V DC Solenoid Actuator* [online]. Distrelec Group Inc., 2021 [visited on 2021-04-02]. Available from: <<https://www.distrelec.biz/en/solenoid-actuator-24vdc-11w-15mm-1n-kuhnke-h6206-24vdc-100-ed/p/15460373>>.
17. HOROWITZ, P.; HILL, W. *The art of electronics*. 3rd Edition. New York: Cambridge University Press, 2015. ISBN 9780521809269.
18. *USB-6001: Multifunction I/O Device* [online]. National Instruments Corporation, 2021 [visited on 2021-04-07]. Available from: <<https://www.ni.com/cs-cz/support/model.usb-6001.html>>.
19. *Comatec PSC 24V DC power supply* [online]. RS Components Limited [visited on 2021-04-09]. Available from: <<https://uk.rs-online.com/web/p/din-rail-power-supplies/8919202/>>.
20. *Comatec PSC 12V DC power supply* [online]. RS Components Limited [visited on 2021-04-09]. Available from: <<https://uk.rs-online.com/web/p/din-rail-power-supplies/8919195/>>.
21. *AD584JNZ - Voltage Reference 10V* [online]. Distrelec Group Inc., 2021 [visited on 2021-04-09]. Available from: <<https://www.elfa.se/en/voltage-reference-10v-10ma-pdip-analog-devices-ad584jnz/p/17322027>>.

22. *GL324 Datasheet* [online]. DatasheetsPDF, 2014 [visited on 2021-04-10]. Available from: <<https://datasheetspdf.com/datasheet/GL324.html>>.
23. *Hongfa HF46F 12V DC power relay* [online]. RS Components Limited [visited on 2021-04-10]. Available from: <<https://uk.rs-online.com/web/p/non-latching-relays/1762804/>>.
24. *IRLZ14PBF N-type MOSFET* [online]. Distrelec Group Inc., 2021 [visited on 2021-04-10]. Available from: <<https://www.elfa.se/en/mosfet-60-10-43-to-220-vishay-irlz14pbf/p/17118805?track=true%5C&no-cache=true>>.
25. *Hongfa HF140FF 12V DC power relay* [online]. RS Components Limited [visited on 2021-04-10]. Available from: <<https://uk.rs-online.com/web/p/non-latching-relays/1762865/>>.
26. *1N4007RLG rectifier diode* [online]. RS Components Limited [visited on 2021-04-10]. Available from: <<https://uk.rs-online.com/web/p/schottky-diodes-rectifiers/6491143/>>.
27. *GP1S094HCZ0F Through Hole Slotted Optical Switch* [online]. RS Components Limited [visited on 2021-04-11]. Available from: <<https://uk.rs-online.com/web/p/slotted-optical-switches/6666518/>>.
28. *GP2L01F Long Focal Distance Type Photointerrupter* [online]. DatasheetsPDF, 2014 [visited on 2021-04-11]. Available from: <<https://datasheetspdf.com/datasheet/GP2L01F.html>>.
29. *DIN connector* [online]. Wikimedia Foundation Incorporated, 2020 [visited on 2021-04-11]. Available from: <https://en.wikipedia.org/wiki/DIN_connector>.
30. BREHM, M.; GRYDLIK, M.; TAYAGAKI, T.; LANGER, G., et al. Photoluminescence investigation of strictly ordered Ge dots grown on pit-patterned Si substrates. *Nanotechnology*. 2015/06/05, **26**. Available from DOI: 10.1088/0957-4484/26/22/225202.
31. BREHM, M.; GRYDLIK, M. Site-controlled and advanced epitaxial Ge/Si Quantum Dots: Fabrication, Properties, and Applications: Fabrication, Properties, and Applications. *Nanotechnology*. 2017/07/21, **28**. Available from DOI: 10.1088/1361-6528/aa8143.
32. GRYDLIK, M.; LANGER, G.; FROMHERZ, T.; SCHÄFFLER, F., et al. Recipes for the fabrication of strictly ordered Ge islands on pit-patterned Si(001) substrates. *Nanotechnology*. 2013/03/15, **24**, 105601. Available from DOI: 10.1088/0957-4484/24/10/105601.
33. GRYDLIK, M.; BREHM, M.; TAYAGAKI, T.; LANGER, G., et al. Optical properties of individual site-controlled Ge quantum dots. *Applied Physics Letters*. 2015/06/22, **106**. Available from DOI: 10.1063/1.4923188.
34. GRYDLIK, M.; LUSK, M.; HACKL, F.; POLIMENI, A., et al. Laser Level Scheme of Self-Interstitials in Epitaxial Ge Dots Encapsulated in Si. *Nano Letters*. 2016/10/05, **16**. Available from DOI: 10.1021/acs.nanolett.6b02494.

35. RAUTER, P.; SPINDLBERGER, L.; SCHAEFFLER, F.; FROMHERZ, T., et al. Room-Temperature Group-IV LED Based on Defect-Enhanced Ge Quantum Dots. *ACS Photonics*. 2017/11/01, **5**. Available from DOI: 10.1021/acsp Photonics.7b00888.
36. SPINDLBERGER, L.; KIM, M.; ABERL, J.; FROMHERZ, T., et al. Advanced hydrogenation process applied on Ge on Si quantum dots for enhanced light emission. *Applied Physics Letters*. 2021/02/22, **118**, 083104. Available from DOI: 10.1063/5.0036039.
37. GROISS, H.; SPINDLBERGER, L.; OBERHUMER, P.; SCHAEFFLER, F., et al. Photoluminescence enhancement through vertical stacking of defect-engineered Ge on Si quantum dots. *Semiconductor Science and Technology*. 2017/01/04, **32**. Available from DOI: 10.1088/1361-6641/aa5697.
38. SCHATZL, M.; HACKL, F.; GLASER, M.; RAUTER, P., et al. Enhanced Telecom Emission from Single Group-IV Quantum Dots by Precise CMOS-Compatible Positioning in Photonic Crystal Cavities. *ACS Photonics*. 2017/02/13, **4**. Available from DOI: 10.1021/acsp Photonics.6b01045.
39. VIJ, D. R. *Luminescence of Solids*. Springer US, 1998. ISBN 978-1-4613-7446-6. Available from DOI: 10.1007/978-1-4615-5361-8.
40. KARPÍŠEK, Z. *Matematika IV: Statistika a pravděpodobnost*. Brno: CERM, 2014. ISBN 978-80-214-4858-2.
41. HALLIDAY, D.; RESNICK, R.; WALKER, J. *Fyzika. Svazek 2*. 2nd edition. Brno: VUTIUM, 2013. ISBN 978-80-214-4123-1.

List of abbreviations

BPM	Beam Profile Monitor
CGS	Centimetre-Gram-Second
DAC	Data Acquisition Card
DC	Direct Current
FC	Faraday Cup
HV	High Vacuum
I/O	Input/Output
MOSFET	Metal Oxide Semiconductor Field Effect Transistor
OS	Operating System
PC	Personal Computer
PCB	Printed Circuit Board
PCI	Peripheral Component Interconnect
PL	PhotoLuminescence
PLC	Programmable Logic Controller
PSU	Power Supply Unit
QD	Quantum Dot
SI	International System of units
TTL	Transistor-Transistor Logic
USB	Universal Serial Bus

List of attachments

Mechanical drawings

Drawing number	Part name	Format
SH-4I	4 inch wafer sample holder	A4
SH-FS	Fluorescent screen holder	A4
GRIP-AS-1	Grip assembly	A3
GRIP-AS-2	Grip assembly part list	A4
GRIP-GB	Grip body	A4
GRIP-GJ	Grip jaws	A4
GRIP-GP	Guiding plate	A4
GRIP-PL	Grip plate	A4
RACK-BP	Rack backplate	A4

Electrical drawings

Drawing number	Part name	Format
CONBO-PL-1	Control board layout 1	A4
CONBO-PL-2	Control board layout 2	A4

Other

Name
T5 Manual
Irradiation parameters
Homogeneity simulation